San Fernando Earthquake Series, 1971: Focal Mechanisms and Tectonics

JAMES H. WHITCOMB, CLARENCE R. ALLEN, JAN D. GARMANY
AND JAMES A. HILEMAN

*Seismological Laboratory, California Institute of Technology
Pasadena, California   91109*

The largest events in the San Fernando earthquake series, initiated by the main shock at 14h 00m 41.8s UT on February 9, 1971, were chosen for analysis from the first three months of activity, 87 events in all. C. R. Allen and his co-workers assigned the main shock parameters: 34°24.7'N, 118°24.0'W, focal depth $h = 8.4$ km, and local magnitude $M_L = 6.4$. The initial rupture location coincides with the lower, northern-most edge of the main north-dipping thrust fault and the aftershock distribution. The best focal mechanism fit to the main shock P wave first motions constrains the fault plane parameters to: strike, N67°(±6°)W; dip, 52°(±3°)NE; rake, 72° (67°–95°) left lateral. Focal mechanisms of the aftershocks clearly outline a down step of the western edge of the main thrust fault surface along a northeast-trending flexure. Faulting on this down step is left lateral strike slip and dominates the strain release of the aftershock series, which indicates that the down step limited the main event rupture on the west. The main thrust fault surface dips at about 35° to the northeast at shallow depths and probably steepens to 50° below a depth of 8 km. This steep dip at depth is a char-acteristic of other thrust faults in the Transverse ranges and indicates the presence at depth of laterally varying vertical forces that are probably due to buckling or over-riding that causes some upward redirection of a dominant north-south horizontal compression. Two sets of events exhibit normal dip slip motion with shallow hypo-centers and correlate with areas of ground subsidence deduced from gravity data. One set in the northeastern aftershock area is related to shallow extensional stresses caused by the steepening of the main fault plane. The other set is probably caused by a deviation of displacements along the down step of the main fault surface that resulted in localized ground subsidence near the western end of the main fault break. Several lines of evidence indicate that a horizontal compressional stress in a north or north-northwest direction was added to the stresses in the aftershock area 12 days after the main shock. After this change, events were contained in bursts along the down step, and sequencing within the bursts provides evidence for an earthquake-triggering phe-nomenon that propagates with speeds of 5–15 km/day. Seismicity before the San Fernando series and the mapped structure of the area suggest that the down step of the main fault surface is not a localized discontinuity but is part of a zone of weakness extending from Point Dume, near Malibu, to Palmdale on the San Andreas fault. This zone is interpreted as a decoupling boundary between crustal blocks that permits them to deform separately in the prevalent crustal shortening mode of the Transverse ranges region.

CONTENTS

1. INTRODUCTION

The main shock of the San Fernando earthquake series occurred on February 9, 1971, in the tectonically active Transverse ranges structural province of Southern California. Immediately following the main shock, the aftershock region was inundated with portable instrumentation from many agencies including the California Institute of Technology (CIT) to make this the most extensively monitored aftershock sequence to date and provide a unique data set for aftershock studies. C. R. Allen et al. (unpublished data, 1972) assigned the main shock parameters as 34°24.7′N, 118°24.0′W, focal depth $h = 8.4$ km, and local magnitude $M_L = 6.4$. The main fault motion, as inferred from observed surface faulting [Kamb et al., 1971; U.S. Geological Survey Staff, 1971], from static displacement of the ground surface [Jungels and Anderson, 1971; Jungels and Frazier, 1973; Alewine and Jordan, 1973], and from the initial focal mechanisms [Division of Geological and Planetary Sciences, 1971; Whitcomb, 1971; Wesson et al., 1971; Dillinger and Espinosa, 1971; Canitez and Toksöz, 1972], was of the thrust type on a north-northeast-dipping fault plane with some left lateral strike slip. The general type and orientation of the main fault plane agree with mapped north-dipping thrust faults that bound many of the southern edges of the Transverse ranges.

From the lunate-shaped distribution of the $M_L = 3.0$ or larger aftershock epicenters shown in Figure 1 and the relatively low seismicity near the surface break [Allen et al., 1971; Hanks et al., 1971; Wesson et al., 1971], it appears that the stresses were completely relieved on the main fault surface and that the larger aftershocks were mainly limited to the edges where stress was concentrated. However, Whitcomb [1971], using focal mechanisms, showed that the apparent lunate symmetry is misleading in that the tectonic pattern along each limb of the distribution is totally different.

Allen et al. (unpublished data, 1972) used the largest aftershocks, mainly those with $M_L = 4.0$ or greater, to formulate a tectonic model of the associated faulting. The focal mechanisms that substantiate the model development are presented first with a review of the model's construction. We then investigate a more extensive set of 87 aftershocks chosen in a uniform manner from the three months between the onset of the series and May 7, 1971. The cutoff date is the time when many of the CIT portable seismometer trailers were removed and the aftershock
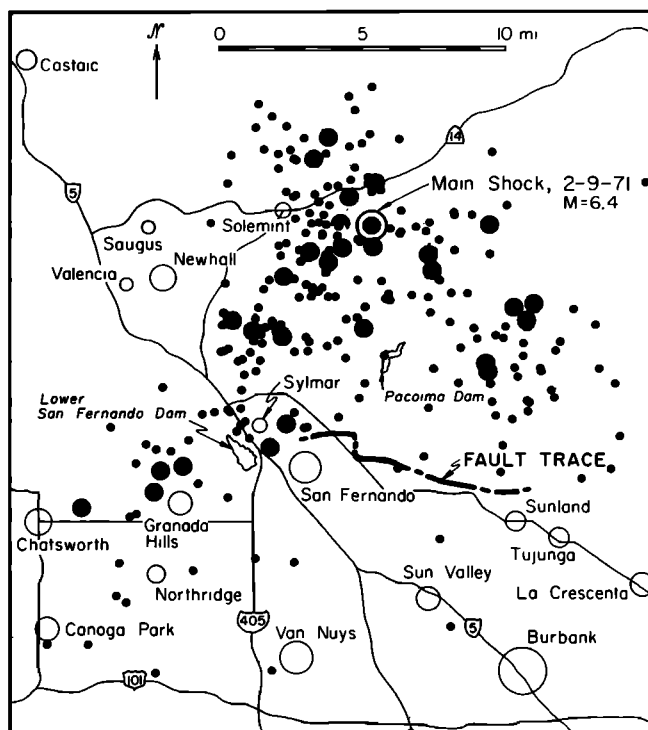
Fig. 1. Epicentral locations of the main San Fernando event
of February 9, 1971, and aftershocks through December 31,
1971. All events of $M_L = 3.0$ or larger, including those not
specially studied, are shown. The larger points indicate events
of $M_L = 4.0$ or larger.

rate had decreased to less than 1/4 days. This second set confirms the general
features of the fault surface model. Some of the individual focal mechanisms and
their locations are obviously not compatible with the model, but this might have
been predicted for a region with such large tectonic movement (up to 2 meters)
[see, e.g., *Burford et al.*, 1971] and such complex geological structure and seis-
micity [*Wentworth et al.*, 1971]. The deviations of the focal mechanisms from
the model-predicted norm are shown to provide additional insight into the time
and spatial variations of the tectonics in the aftershock region. We then inves-
tigate isolated bursts of activity occurring later in the series, which suggest a
propagating phenomenon that triggers events. Last, we relate the pre-1971
seismicity and the mapped structure in the region to the tectonic features of
the San Fernando earthquake series.

2. DATA SET

A major goal of aftershock studies is to outline the associated tectonics of
the region. It is therefore desirable to choose the set of aftershocks that is most
representative of the major tectonic stress release. This means that the after-

shock set must contain the largest events. A practical limit is set at the lower end of the magnitude scale owing to a limit on the size of the data set and the signal strengths that the stations record. From this reasoning, the aftershock set that is most representative of the regional tectonic activity includes all events above a certain size.

Two definitions of cutoff size are used. The first set is defined as all aftershocks of $M_L = 4.0$ or larger. P wave first motions that are immersed in the coda of previous shocks are not used, and this unfortunately precludes the use of events during the first hour of the aftershock series. But the set is complete after the first hour, giving a total of 20 events. A histogram of all aftershocks of $M_L = 4.0$ or larger is shown in Figure 2a. The dark portions indicate the events in the first set.

The second set is defined as those shocks whose P wave first motions are clear on most of the CIT permanent stations, most of which are between 90 and 300 km from the epicenters. The rationale for this definition is that the data from the more distant stations are much less sensitive to hypocentral location and velocity errors than data from the close-in portable stations when their first motions are mapped onto the focal hemisphere. Again, the homogeneity of the aftershock set is compromised by the occasional immersion of first motions in the coda of a previous shock. This occurs most often during the first few hours of the aftershock series, and its effect on the conclusions cannot be esti-
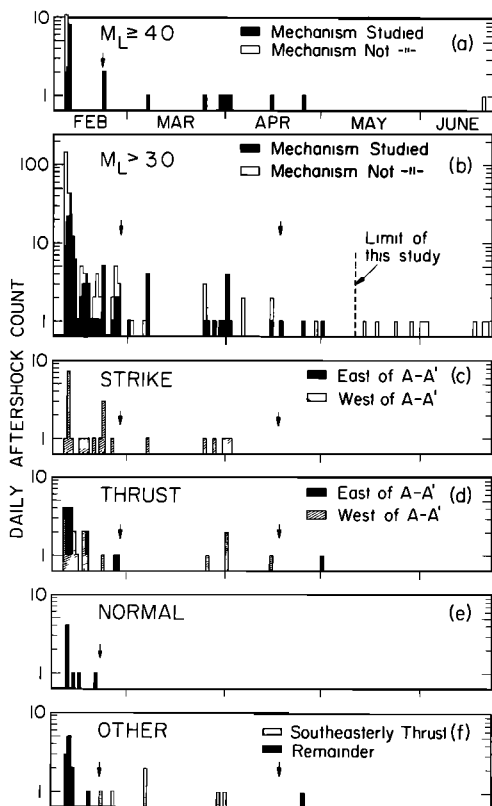

Fig. 2. Histograms of the aftershock groups: (a) M_L of 4.0 or greater, (b) M_L greater than 3.0, (c) strike slip events that fit the model, (d) thrust events that fit the model, (e) events with normal dip slip, and (f) others.

mated. One can only assume that the masking is distributed randomly with aftershock type and that the stress release during the first few hours is not basically different except in rate from the remainder of the series. Some of the conclusions reached below deal with the latter assumption. A histogram of the aftershocks with M_L larger than 3.0 is shown in Figure 2b. The dark portions indicate the events included in the second set.

Table 1 lists all the events of the second set, which of course includes the first

TABLE 1. Aftershock Events of Sets 1 and 2

No.	Date 1971	Time, UT	M_L	Epicenter 34°N	118°W	Depth	Loca-tion Quality	Focal Mechanism Quality	First-Motion Stations
Main	Feb. 9	14h 00m	6.4	24.7'	24.0'	8.4	B*	B	101
1	Feb. 9	15h 10m	3.9	24.8'	24.7'	8.	C†	C	7
2	Feb. 9	15h 38m	3.9	24.4'	28.0'	8.	C†	B	12
3	Feb. 9	15h 58m	4.8	22.46'	20.10'	9 0	B*	C	12
4	Feb. 9	16h 19m	4.2	27.44'	25.62'	−1.	C*	B	12
5	Feb. 9	17h 03m	3.9	22.2'	29.5'	8.	C†	B	10
6	Feb. 9	17h 19m	3.6	24.7'	26.8'	8.	C†	B	12
7	Feb. 9	18h 29m	3.8	23.7'	28.9'	8.	C†	C	13
8	Feb. 9	20h 53m	3.4	26.1'	23.7'	8.	C†	A	15
9	Feb. 9	20h 56m	3.7	18.5'	21.3'	8.	C†	B	11
10	Feb. 10	01h 38m	3.9	19.3'	32 0'	8.	C†	B	17
11	Feb. 10	03h 12m	4.0	22.20'	18.12'	0.8	B*	A	18
12	Feb. 10	05h 06m	4.3	24.67'	19.76'	4.7	B*	C	19
13	Feb. 10	05h 18m	4.5	25.55'	24.85'	5.8	B*	C	20
14	Feb. 10	05h 41m	3.7	21.6'	17.8'	8.	C†	A	16
15	Feb. 10	06h 24m	3.4	24.4'	19.5'	8.	C†	A	12
16	Feb. 10	06h 54m	3.4	23.7'	27.0'	8.	C†	C	13
17	Feb. 10	07h 00m	3.5	18.1'	18.5'	8.	C†	A	14
18	Feb. 10	07h 14m	3.4	21.4'	26.5'	8.	C†	A	18
19	Feb. 10	07h 27m	3.8	24.1'	26.1'	8.	C†	C	17
20	Feb. 10	09h 33m	3.2	19.6'	15.2'	8.	C†	A	16
21	Feb. 10	10h 00m	3.4	26 8'	27.7'	8.	C†	B	19
22	Feb. 10	11h 29m	3.2	27.2'	25.6'	8.	C†	B	20
23	Feb. 10	11h 31m	4.2	23.06'	27.30'	6.0	B*	A	20
24	Feb. 10	11h 45m	3.5	23.4'	28.5'	8.	C†	A	20
25	Feb. 10	12h 42m	3 4	20.7'	16.9'	8.	C†	A	18
26	Feb. 10	13h 49m	4.3	23 94'	25.12'	9 7	A*	B	21
27	Feb. 10	14h 35m	4 2	21.69'	29.20'	4.4	A*	A	22
28	Feb. 10	17h 38m	4.2	23.74'	21.98'	6.2	A*	B	20
29	Feb. 10	18h 54m	4.2	26.75'	26.16'	8.1	A*	B	21
30	Feb. 10	19h 06m	3.5	22.51'	18.07'	11.3	B	A	21
31	Feb. 10	23h 42m	3.5	23.14'	21.41'	8.1	B	C	22
32	Feb. 11	00h 30m	3.5	24.50'	16.63'	5.0	B‡	B	24
33	Feb. 11	03h 43m	3.2	25.05'	26.32'	8.0	A	B	25
34	Feb. 11	04h 07m	3.4	18.39'	32.13'	11.3	B‡	B	22
35	Feb. 11	07h 33m	3.3	27.41'	26.50'	12.4	A	A	22
36	Feb. 11	09h 24m	3.3	24.91'	20 34'	5.0	B‡	B	26
37	Feb. 11	11h 32m	3 5	20.20'	18.83'	0.5	A‡	B	26
38	Feb. 11	14h 21m	3.5	17.78'	19.28'	2.4	B	B	26
39	Feb. 11	16h 43m	3.6	22 07'	27.70'	2 3	A	A	23
40	Feb. 11	19h 35m	3.7	24.00'	26.87'	6.4	A	B	26

TABLE 1. (continued)

No.	Date 1971	Time, UT	M_L	Epicenter 34°N	Epicenter 118°W	Depth	Location Quality	Focal Mechanism Quality	First-Motion Stations
41	Feb. 11	23h 35m	3.7	21.11′	20.21′	4.6	A	B	25
42	Feb. 12	08h 09m	3.2	21.56′	21.28′	1.8	B	B	24
43	Feb. 12	09h 20m	3.3	25.56′	25.73′	8.1	A	A	27
44	Feb. 12	09h 52m	3.4	21.55′	27.18′	2.0	A	A	26
45	Feb. 12	15h 02m	3.4	24.41′	25.86′	9.5	B	A	25
46	Feb. 12	16h 22m	3.9	24.77′	25.50′	9.2	A	A	26
47	Feb. 13	06h 44m	3.2	19.64′	32.80′	1.6	B	A	28
48	Feb. 14	03h 38m	3.3	23.86′	23.03′	9.4	A	A	23
49	Feb. 14	13h 44m	3.8	17.97′	30.67′	1.1	B	A	30
50	Feb. 15	08h 04m	3.9	28.27′	24.63′	12.9	A	A	27
51	Feb. 15	08h 46m	3.4	24.42′	26.48′	7.9	A	A	23
52	Feb. 15	13h 03m	3.4	25.65′	26.12′	9.7	A	A	22
53	Feb. 16	04h 37m	3.5	17.25′	32.61′	0.6	B	A	25
54	Feb. 16	07h 08m	3.3	24.40′	26 86′	9.3	A	B	22
55	Feb. 16	14h 39m	3.1	20.07′	17.87′	10.0	A	A	23
56	Feb. 17	10h 15m	3.5	21.46′	18.38′	5.3	A	B	20
57	Feb. 18	22h 09m	3.2	23.18′	25.85′	4.4	A	A	17
58	Feb. 19	02h 45m	3.5	21.45′	27.58′	−1.5	B	B	22
59	Feb. 20	08h 09m	3.6	27.24′	24.38′	15.2	A	B	21
60	Feb. 21	02h 42m	3.6	17.69′	31.86′	6.8	B	A	20
61	Feb. 21	05h 50m	4.7	23.85′	26.32′	6.9	A*	A	27
62	Feb. 21	07h 15m	4.5	23.52′	25.65′	7.2	A*	A	26
63	Feb. 21	07h 43m	3.5	23.87′	25.58′	4.9	A	A	21
64	Feb. 21	14h 06m	3.5	23.89′	26.70′	6.2	A	A	19
65	Feb. 24	16h 04m	3.7	26.48′	24.64′	10.8	A	A	21
66	Feb. 25	11h 27m	3.2	25.23′	26.51′	7.5	A	B	17
67	Feb. 25	20h 27m	3.5	20.17′	21.79′	−2.0	B	A	20
68	Feb. 26	03h 33m	3.5	25.13′	22.95′	7.5	A	A	20
69	Feb. 26	21h 22m	3.3	27.25′	27.21′	10.0	A	C	18
70	Mar. 1	04h 28m	3.4	24.05′	26.00′	4.4	A	C	19
71	Mar. 7	01h 33m	4.5	21.19′	27.35′	3.2	A*	A	33
72	Mar. 7	06h 56m	3.9	22.59′	26.00′	4.9	A	C	27
73	Mar. 7	07h 11m	3.3	22.65′	26.22′	0.8	A	B	23
74	Mar. 25	21h 36m	3.3	24.83′	22.85′	3.8	A	B	25
75	Mar. 25	22h 54m	4.2	21.38′	28.47′	4.6	A*	A	28
76	Mar. 26	20h 55m	3.3	28.09′	27.68′	11.3	A	A	19
77	Mar. 28	17h 16m	3.7	21.28′	28.39′	5.7	A	A	28
78	Mar. 30	08h 54m	4.1	17.74′	27.84′	2.6	A*	A	29
79	Mar. 31	14h 52m	4.6	17.15′	30.89′	2.1	A*	A	30
80	Apr. 1	01h 54m	3.4	15.94′	35.34′	6.3	B	B	23
81	Apr. 1	15h 03m	4.2	24.72′	25.19′	7.1	A*	A	31
82	Apr. 1	21h 15m	3.2	24.32′	25.85′	7.9	A	A	21
83	Apr. 1	21h 18m	3.5	23.73′	25.73′	7.3	A	B	28
84	Apr. 2	05h 40m	4.0	17.03′	31.70′	3.0	A*	A	30
85	Apr. 15	11h 14m	4.2	15.88′	34.62′	4.2	A*	A	28
86	Apr. 25	14h 48m	4.0	22.09′	18.86′	−2.0	B*	A	20
87	May 1	04h 25m	3.6	26.00′	24.15′	4.8	A	A	22

* Location from C. R. Allen et al. (unpublished data, 1972).
† Location modified from *Allen et al.* †[1971].
‡ Location from *Hanks et al.* [1971].

set, along with local magnitude, location, location quality, focal mechanism quality, and number of stations used for first-motion determinations (most of these parameters are discussed below). The smallest shock that fulfills the criterion of first-motion clarity at most of the CIT telemetry stations has an M_L of 3.1. Essentially all shocks with an M_L of 3.5 or larger fulfill the criterion and are included unless masked by a previous shock. The histogram of Figure 2b shows that most of the aftershocks above $M_L = 3.0$ after the first two days have first motions that are clear enough to be included in the second set, which can be considered to have an approximate magnitude cutoff of $M_L = 3.3$.

The stations used for P wave first motions in this study, with their operating agencies, coordinates, and periods of operation, are given in Table 2. The station

TABLE 2.   Stations Used for P Wave First Motions

Station	Agency	Latitude North	Longitude West	Period of Operation
AGM	EML	34°29.5′	118°19.3′	Feb. 10–Apr. 24, 1971
ANM	EML	34°27.2′	118°30.6′	Mar. 15–Apr. 24, 1971
BAR	CIT	32°40.8′	116°40.3′	Permanent
BHR	USC	34°00.5′	118°21.7′	Feb. 27, 1971–present
BLA	CIT	34°14.8′	118°26.7′	Mar. 2, 1971–present
BQR	CIT	34°17.6′	118°35.4′	Feb. 9–May 7, 1971
BRC	CIT	34°17.6′	118°35.4′	Feb. 9–May 7, 1971
BRCL	LGO	34°23.0′	117°46.3′	Feb. 12–14, 1971
CLC	CIT	35°49.0′	117°35.8′	Permanent
CSP	DWR	34°17.9′	117°21.5′	Permanent
CWC	CIT	36°26.4′	118°04.7′	Permanent
ENG	CIT	34°08.4′	118°05.2′	Semi-permanent
GLA	CIT	33°03.1′	114°49.6′	Permanent
GOK	CIT	34°23.1′	118°28 3′	Feb. 10–May 6, 1971
GOR	LGO	34°46.9′	118°48.0′	Feb. 10–14, 1971
GSC	CIT	35°18.1′	116°48.3′	Permanent
HAY	CIT	33°42.4′	115°38.2′	Permanent
HCC	USC	33°59.6′	118°23.0′	Feb. 28, 1971–present
IND	CIT	34°25.2′	118°16.2′	Feb. 10–Apr. 22, 1971
IPC	USC	33°58.2′	118°20.4′	Mar. 4, 1971–present
IRC	CIT	34°23.3′	118°23.9′	Feb. 9–May 7, 1971
ISA	CIT	35°38.6′	118°28.6′	Permanent
JBF	USC	33°59.6′	118°20.7′	Mar. 25, 1971–present
LSV	LGO	34°36.4′	118°19.5′	Feb. 10–12, 1971
MER	LGO	34°29.8′	118°02.4′	Feb. 12–14, 1971
MLM	EML	34°23.4′	118°04.8′	Feb. 10–Apr. 24, 1971
MWC	CIT	34°13.4′	118°03.5′	Permanent
OMM	EML	34°19.8′	118°36 0′	Feb. 25–Apr. 24, 1971
PAS	CIT	34°08.9′	118°10.3′	Permanent
PLM	CIT	33°21.2′	116°51.7′	Permanent
PYR	DWR	34°34.1′	118°44.5′	Permanent
RTM	EML	34°35.8′	118°14.8′	Feb. 10–Mar. 15, 1971
RTR	CIT	34°11.9′	118°09 4′	Semi-permanent
RVR	CIT	33°59.6′	117°22.5′	Permanent
SBC	CIT	34°26.5′	119°42.8′	Permanent
SCF	NOS	34°26.3′	118°17.3′	Feb. 10–17, 1971
SGM	NOS	34°23.1′	118°24.8′	Feb. 10–17, 1971

TABLE 2.   (continued)

Station	Agency	Latitude North	Longitude West	Period of Operation
SHC	NOS	34°30.5′	118°21.8′	Feb. 10–17, 1971
SOC	CIT	34°26.1′	118°21.7′	Feb. 10–May 6, 1971
SWM	CIT	34°43.0′	118°35.0′	Permanent
SWML	LGO	34°42.1′	118°32.1′	Feb. 10–14, 1971
SYP	CIT	34°31.6′	119°58.7′	Permanent
TIN	CIT	37°03.3′	118°13.7′	Permanent
USC	USC	34°00.8′	118°17.3′	Feb. 6–28, 1971
USCB	USC	34°00.1′	118°20.5′	Feb. 12–14, 1971
USCP	USC	34°02.7′	118°32.1′	Feb. 12–14, 1971
WSM	EML	34°36.4′	118°33.5′	Feb. 10–Apr. 24, 1971

CIT, California Institute of Technology; DWA, California Department of Water Resources; EML, Earthquake Mechanisms Laboratory, NOS; LGO, Lamont-Doherty Geological Observatory; NOS, Las Vegas Branch of National Ocean Survey; USC, University of Southern California.

locations in relation to the approximate epicentral distribution of aftershocks (Allen et al., unpublished data, 1972) are shown in Figure 3. All readings were made from short-period vertical seismometers. Although 47 stations were used for first-motions studies, varying periods of operation for the portable stations and the weakness of the first arrival of smaller shocks at distant stations reduced the actual number of first motions read per event. The number of readings for most events ranged from 10 to 20 for the first twenty hours of the aftershock series and from 20 to 30 for the remainder of the study time period. Some instrument polarity reversals did appear, usually in instrumentation that was temporary
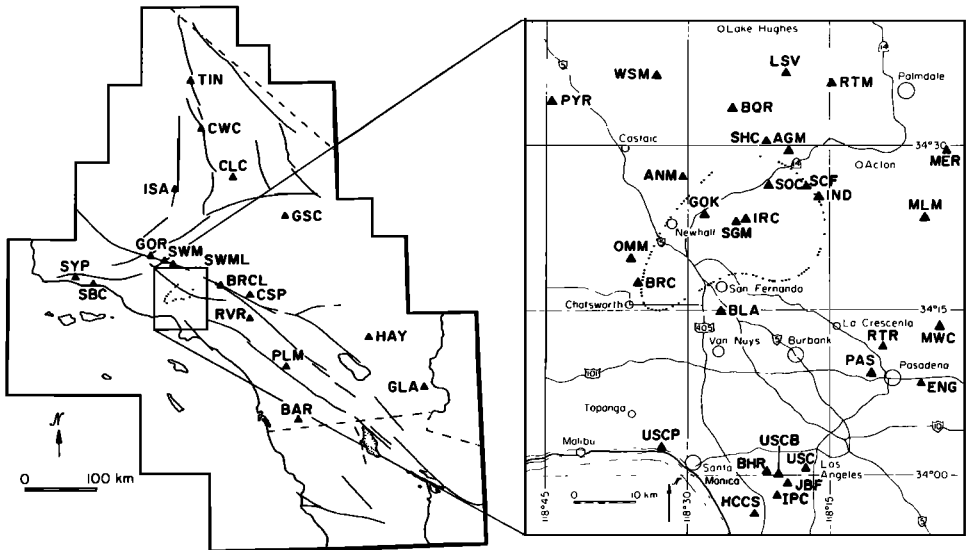
Fig. 3.   Location map of stations used for first-motion studies; station data are listed in Table 2. The approximate aftershock zone is shown for reference.

or that involved complex electronics such as a telemetry link from seismometer to recorder. However, the station coverage and the number of events were sufficient to reveal the reversal. Also, in almost every case, a reversal could be confirmed by polarity checks with teleseismic events.

3. HYPOCENTRAL LOCATIONS

The hypocentral locations done by us are computed with the same method as that used by Allen et al. (unpublished data, 1972), except that the closer stations are weighted more heavily, especially for shallow hypocenters. The stations used for locations are those of CIT and the Earthquake Mechanisms Laboratory (EML), shown in Figure 3 and Table 2, and in some cases SUS, which is a station of the United States Geological Survey's National Center for Earthquake Research [see *Wesson et al.*, 1971]. For shocks in the western extremity of the after-shock region, the westerly stations BRC, OMM, and SUS are given large weights to offset the bias introduced by the fact that most of the close stations lie to the east. Because the aftershocks in the set are all larger than $M_L = 3.0$, S wave arrival times are difficult to measure on the high-gain film records of the CIT portable stations. These S wave arrival times that are read from the CIT stations and those listed in the EML data reports are given half the weight of their associated P wave arrival times.

In the earlier part of the aftershock sequence, approximately the first 24 hours, not enough portable stations were in place for precise hypocentral locations. Allen et al. recomputed the locations of the events with $M_L = 4.0$ or larger in this early period by applying time correction factors to arrival times from the permanent southern California stations. The corrections were computed from precise locations of later shocks by use of the portable stations. The locations taken from Allen et al. (unpublished data, 1972) are indicated with stars in Table 1. The remainder of the locations in this early period are from *Allen et al.* [1971], with some modification to account for systematic epicentral shifts that are present when comparing locations from only the permanent station data with those from the closer portable station data. The modified locations are indicated in Table 1 with dagger symbols. Four of the event hypocenters have been computed by *Hanks et al.* [1971] and are indicated by double daggers in Table 1. The remaining locations were computed by us.

The accuracy of the hypocenters in this study is estimated by following the definitions of Allen et al. (unpublished data, 1972). On the basis of the number and location of the stations and the standard error of the computer solution, the quality of the hypocentral locations is indicated in three categories: 'A' locations are generally accurate to within 2 km horizontally and 4 km vertically; 'B' locations are felt to be accurate to within 4 km horizontally and 8 km vertically; and 'C' locations include all those that are considered less accurate. The location qualities are given in Table 1. As can be seen by the definitions, the accuracy of the epicentral determination is much better than that of the depth; this is especially true for those events with shallow depths. Direct confirmation of the location accuracies is extremely difficult short of drilling down and firing a large explosive

at hypocentral depths. However, the accuracies estimated for the different quali- ties are considered conservative on the basis of variations of the hypocenter as a function of reasonable changes of velocities, station corrections, station com- bination, and station weighting. Because all the A and B quality events are located in essentially the same manner, hypocenters in the same region should be located more accurately relative to each other than is implied by the above estimates of absolute location accuracy.

4. FOCAL MECHANISM DETERMINATIONS

P wave first motions are used exclusively for the focal mechanism deter- minations. The first-motion reading is classified as good or fair depending on a subjective estimate of the onset clarity and on how confident we are that the motion is truly the first arrival; doubts in the latter situation occur most often at distances where P_n is the first arrival. A record is also kept of arrivals that have emergent character when, by a subjective judgment involving the epicentral distance and size of the aftershock, one would expect the first motion to be sharp; these arrivals are designated as having nodal character, implying that they map on the focal sphere near one of the nodal planes of the double couple. Although this character is not used in the fit of the double-couple mechanism to the data, it is found that these points indeed tend to map near the nodal planes. It is therefore believed that, with proper precautions, they can be used in future studies as additional information in a focal mechanism fit.

The source takeoff angle is calculated by ray tracing as a function of the aftershock's epicentral distance and depth by using the P wave velocity model shown in Figure 4. The model is based mainly on the results of *Healy* [1963], who analyzed a reversed refraction profile between Santa Monica Bay and Camp Roberts, California, that passes very close to the epicentral area. Take- off angles were calculated also for the velocity model shown as a dashed line in Figure 4, which includes a 7.2 km/sec layer at the base of the crust. How- ever, the rays refracted along the top of this layer were first arrivals for only a very small epicentral distance range, which made the difference between the two velocity models insignificant. This is especially true in light of the large
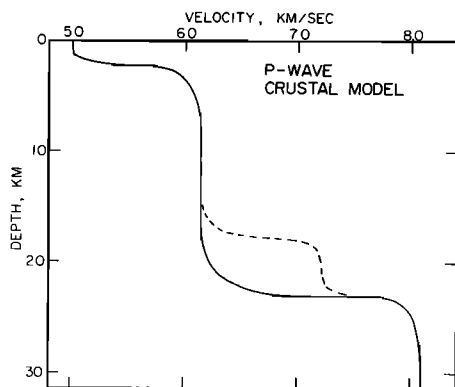
Fig. 4. P wave velocity distribution used to map the first-motion data onto the focal sphere. The dashed line indicates a variation of the velocity that produced no significant changes in the mapping.

lateral variations in shallow crustal structure demonstrated by *Wesson and Gibbs* [1971]. These variations probably have much greater effect on the ray takeoff angles and azimuths, and if one were to use a more sophisticated velocity model, lateral variations should be included. The use of the more distant stations helps to minimize these effects because the rays leaving the hypocenter in a downward direction presumably encounter less drastic lateral changes in velocity. Wesson and Gibbs's results generally confirmed the shallow part of *Healy's* [1963] model with crystalline basement rock velocities of around 6 km/sec. Although Wesson and Gibbs obtained near-surface sediment velocities in the Santa Susana mountains as low as 3.4 km/sec, this velocity is not used here in the focal mechanism computations for shallow hypocenters in the southwest aftershock region. The initial ruptures of the larger aftershocks would be in the stronger, and therefore higher-velocity, rocks because they support most of the stress. Thus, the shallow hypocenters, which are always the most inaccurate, are assumed to be deep enough to be in higher-velocity sedimentary or crystalline rock.

The focal mechanism of the main shock has been recomputed by using some new close-in station data and estimates of the P_g-P_n breakover distance based on the aftershock data at stations near this range. The best fit to the P wave first-
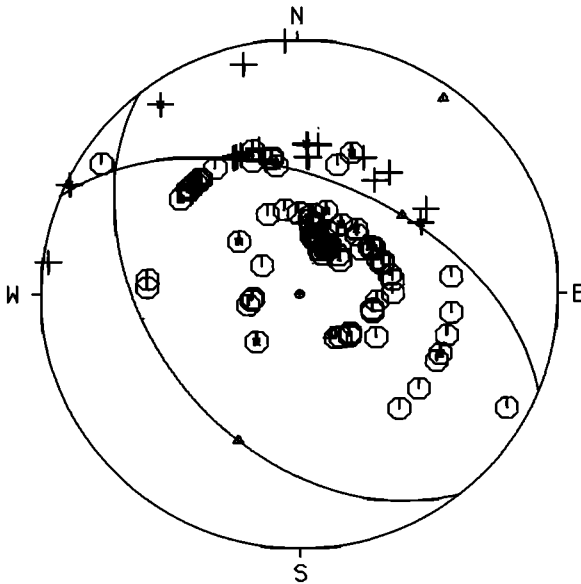
Fig. 5. The main February 9, 1971, San Fernando shock first-motion data and the best fit of the double-couple mechanism. The data are shown on an equal-area projection of the lower focal hemisphere. Circles denote compressions (large size, good reading qualities; small size, fair reading qualities). Crosses denote dilatations (large size, good reading qualities; small size, fair reading qualities). Stars indicate nodal character; triangles indicate slip vectors, compression axis, and tension axis.
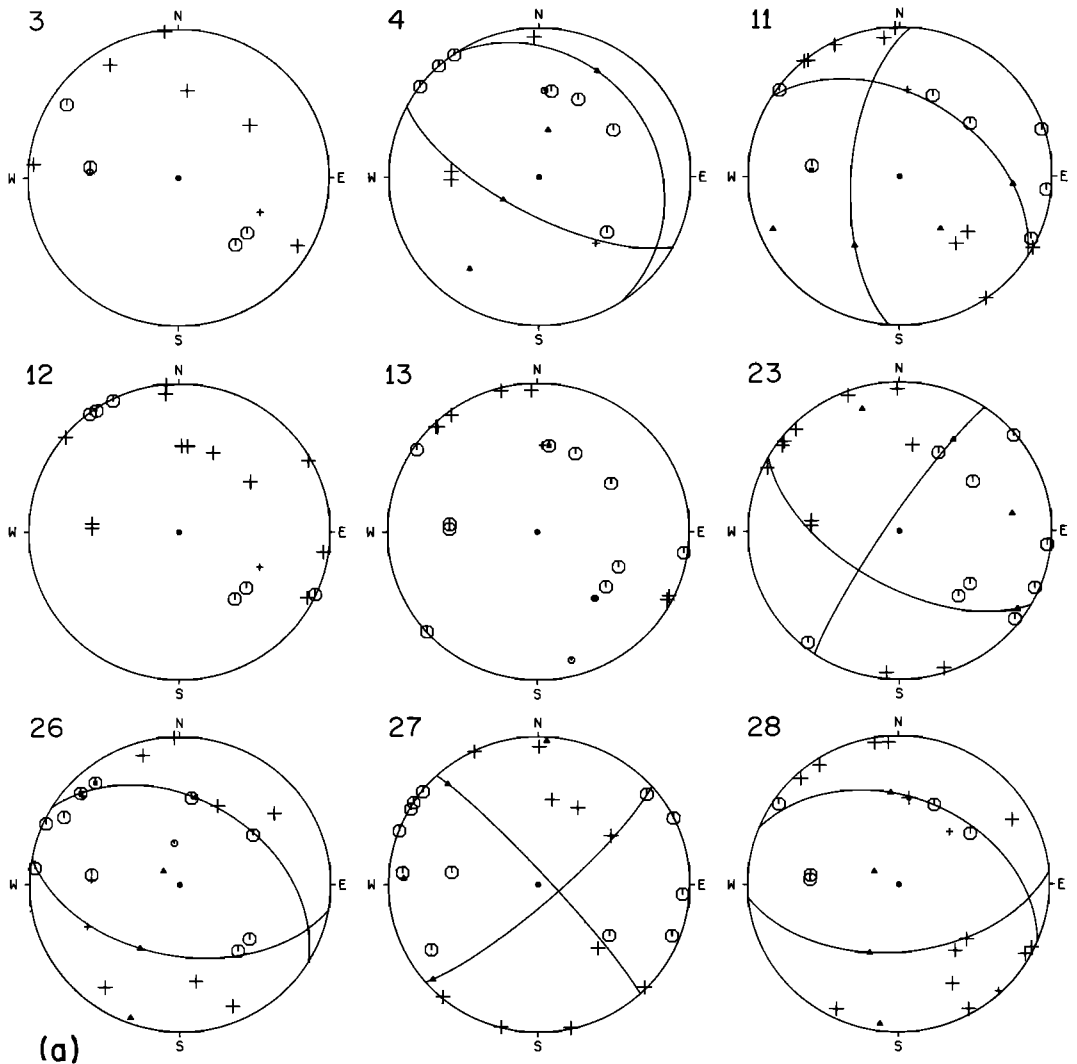
(a)

⊙ ∘ Compression (Good, Fair)   * Nodal Character
+ + Dilatation (Good, Fair)   ▲ Slip Vectors, T Axis, C Axis

Fig. 6a.

Fig. 6.   First-motion data and their focal mechanism fits for aftershocks of $M_L = 4.0$ or greater. Numbers correspond to events in Table 1. Data are shown on an equal-area projection of the lower focal hemisphere.

motion data constrains the fault plane parameters to: strike, N67°($\pm6°$)W; dip, 52°($\pm3°$)NE; and rake, 72° (67°–95°) left lateral. Choice of the northeast-dipping plane as the fault plane rather than the auxiliary plane is based on its close correspondence to the observed surface faulting, the hypocentral locations
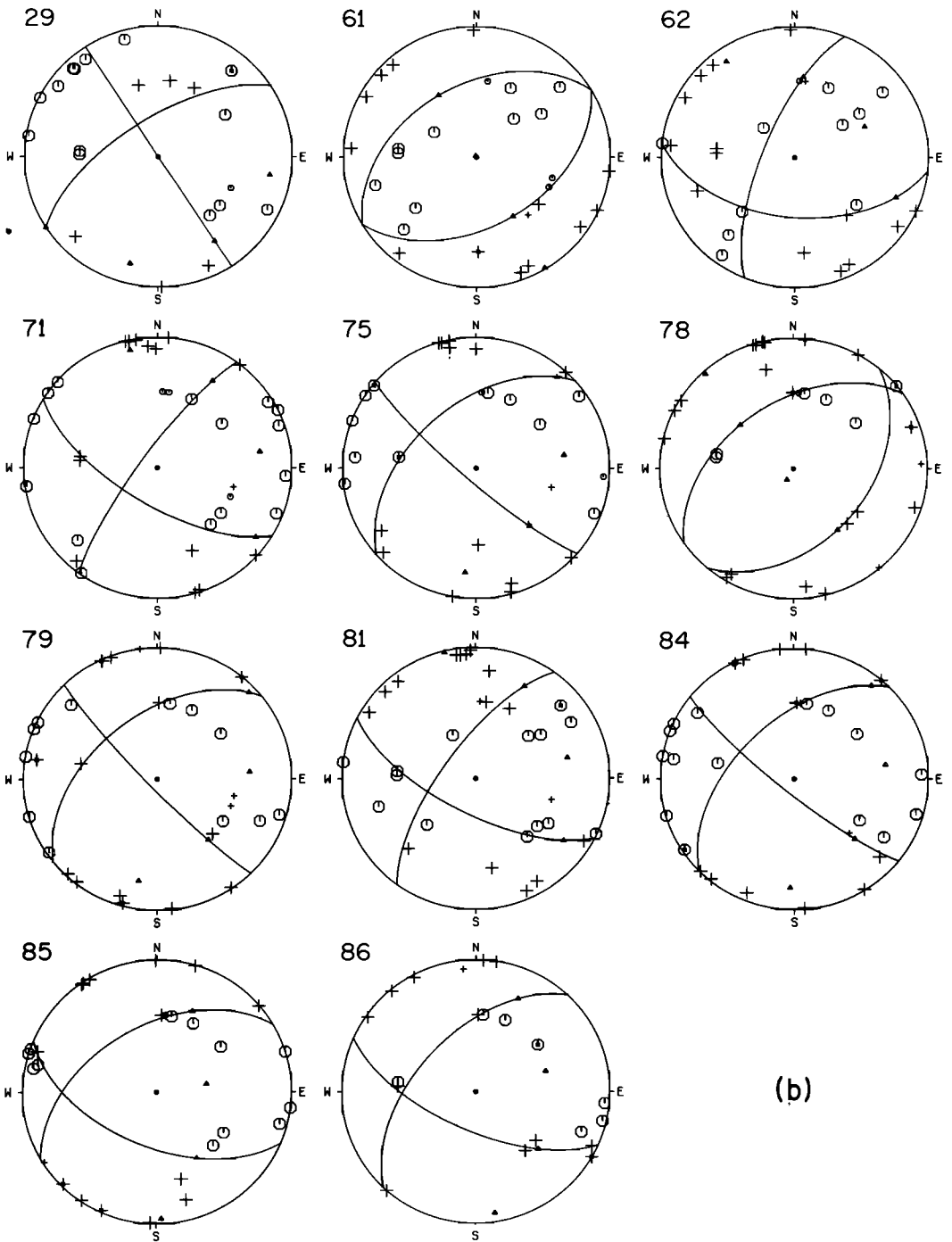
Fig. 6b.

of aftershocks, and the regional geology. The best fit is determined by minimizing the reading misfits to a double couple with an algorithm that will be described in a later paper. The fit to the data is shown in Figure 5. It is interesting to note that the fault plane is very well determined but that the rake angle, which is tied to the auxiliary plane, is much less so; this illustrates that station distributions can selectively constrain some focal mechanism parameters much better than others.

Canitez and Toksöz [1972] have estimated the rake angle from surface waves to be 45°, which would indicate a much greater average strike slip over the fault plane than the strike slip of the initial rupture and, as seen later, of the aftershocks. However, the determination was made by using only six stations covering one quadrant at the source, and the effects of varying crustal structures were not calculated for the surface wave paths. Thus, although their rake is interesting and has important implications, we prefer to withhold an attempt to explain this deviation pending a more complete confirmation of the value.

The double-couple focal mechanisms of the aftershocks are fitted to the data by eye under the influence of the reading qualities, good or fair. An estimate of the quality of the solution is made on the basis of the degree to which data constrain the orientation of the solution. Category A solution parameters are felt to be within 10° of the actual values, and B solution parameters are felt to be within 20°; C events are all others and are not assigned a solution. These definitions are intended to apply to the worst-constrained parameters of the solution.

Figure 6 shows data for all aftershocks with $M_L = 4.0$ or larger; the plots include first-motion data and the focal mechanism solutions mapped on equal-area stereo plots of the lower focal hemisphere. The event numbers correspond to those in Table 1. Although it is impractical to show equivalent plots for all 87 events, the set in Figure 6 includes examples of all three focal mechanism quality ratings.

5. TECTONIC INTERPRETATION

a. Magnitude 4.0 or larger shocks and development of a fault model. As defined above, the first set of aftershocks consists of those with an $M_L = 4.0$ or larger. The fits of focal planes to the first-motion data shown in Figure 6 are transformed to schematic diagrams of the quadrants in the lower focal hemisphere delineating the areas of compressional (dark) and dilatational (light) first motions and are shown at their epicentral locations in Figure 7. The larger diagrams denote A quality focal mechanisms, and the smaller denote B quality. Three of the twenty events have C quality focal mechanisms with no determination of the planes, but their epicentral locations are included in the figure. This set is complete after the first hour of the series, and Figure 7 shows that most of the activity of these largest shocks is on the western limb, which is separated approximately from the rest of the aftershock sequence by the line A-A'. It is also apparent that over half of the focal mechanisms along the western limb have a steeply dipping plane striking northeast parallel to the limb direction with left
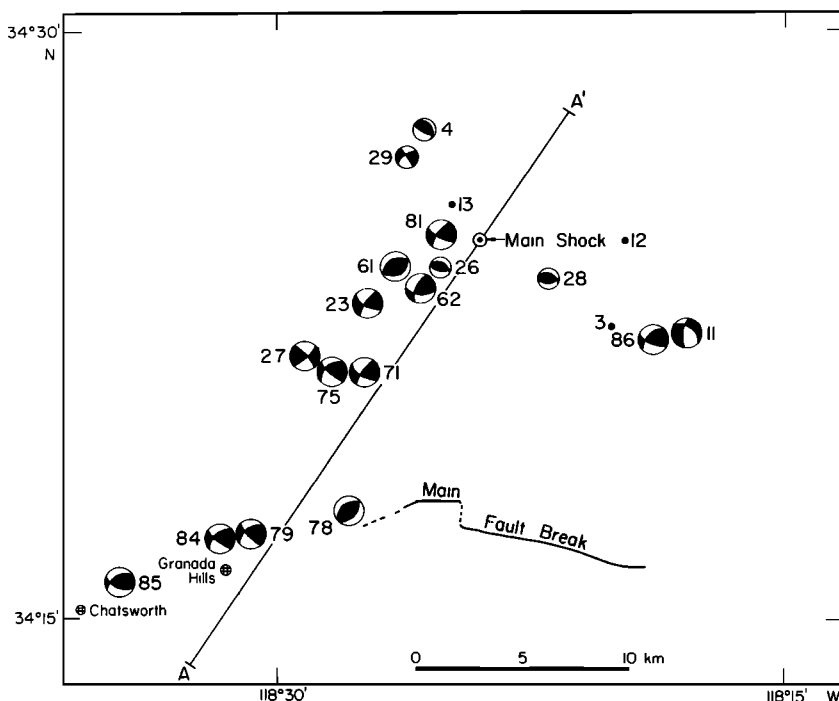
Fig. 7. Aftershocks of $M_L = 4.0$ or greater as schematic diagrams of the compressional (dark) and dilatational (light) first-motion quadrants in the lower hemisphere. The diagrams are at the event's epicenters, and the numbers refer to those in Table 1. The size of the diagram refers to its focal mechanism quality A (larger) or quality B (smaller; see text). All events with A and B quality focal mechanisms are included, and the locations of three C quality mechanisms are indicated by points (events 3, 12, and 13).

lateral strike slip fault motion. If these strike slip mechanisms are connected to a single surface that is related to the tectonic motion of the main shock, then the strike slip surface must be below the main thrust fault plane defined by the surface rupture, focal mechanism, and hypocenter of the main shock. If the strike slip surface were above the main fault plane, the motion would be right lateral for northeast striking faults, contrary to the observed motion. This distribution of focal mechanisms can be explained by the fault surface model first presented in unpublished data of C. R. Allen et al. (1972) and shown in Figure 8. It was based on many of these same data. The figure is a schematic structural contour map showing simplified contours, in kilometers, on the fault plane. The fault surface associated with the main thrust rupture is in the eastern portion of the map. In the vicinity of the western limb of aftershocks, the surface has a steep flexure that is down-stepped to the west and is associated with left lateral strike slip motion. This flexure tended to limit the initial rupture to the west, and, because of the resulting stress concentration in this zone, it was responsible for most of the aftershock activity. Two events, numbers 4 and 85 in Figure 7, are on the western edge of the western limb of aftershocks, but their mechanisms are
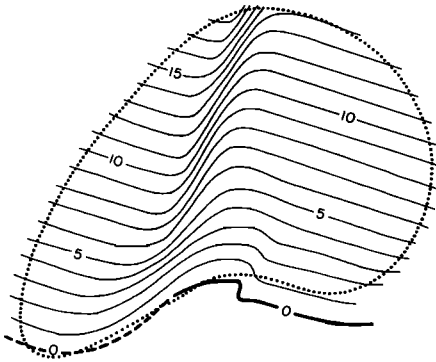
Fig. 8. San Fernando fault surface model showing the surface as simplified contours, in kilometers, with a down step to the west that explains the strike slip events along the west limb of the aftershock zone (Allen et al., unpublished data, 1972).

mainly thrust, similar to those of the main shock. These events can be explained by the flattening of the surface to the west, as shown in Figure 8. However, the model requires that the thrusts west of the flexure be deeper than those to the east; this is one of the important hypotheses to be tested with the second aftershock set.

  b. *Test of the model with the second aftershock set.* The fault model developed for the twenty $M_L = 4.0$ or larger shocks should be representative of the major strain release of the aftershock series. The second and larger set of 87 aftershocks, including smaller events, can now be analyzed with the model as a test framework.

  Figure 9 presents all the A and B quality focal mechanisms that agree with the model of Figure 8. As before, they are shown as a map of schematic diagrams of the compressional (dark) and dilatational (light) first-motion quadrants in the lower focal hemisphere. The epicentral locations may be slightly in error because of crowding in the figure. Two-thirds (50/75) of the A and B focal mechanisms are included in Figure 9; certainly this represents strong support for the fault model of Figure 8. Certain characteristic features noted in Figure 6 are preserved here in Figure 9. Most of the activity is in the well-defined western limb of the aftershock sequence. Half of these events in the western limb have a plane dipping steeply to the northwest and striking to the northeast roughly parallel to the limb, and the motion on the planes is predominantly left lateral strike slip. The criterion for designating these aftershock focal mechanisms as mostly strike slip or thrust is simply whether the rake (the angle in the fault plane between horizontal and the slip vector) is less than or greater than 45°, respectively. Although it appears that some thrust events appear to map within the western limb, a more complete location analysis done below shows that the thrusts in this area clearly tend to occur deeper and to the west of the strike slip events.

  The histograms of the thrust and strike slip events that agree with the model are shown in Figures 2c and 2d. There is little difference in their overall time distribution, but if they are separated into east and west regions by A-A′ (as indicated by different shading in the figure), they show that the model-related events east of A-A′ larger than $M_L = 3.0$ are absent after the first 18 days of the series for two months. Thus at least two and perhaps three prelimi-
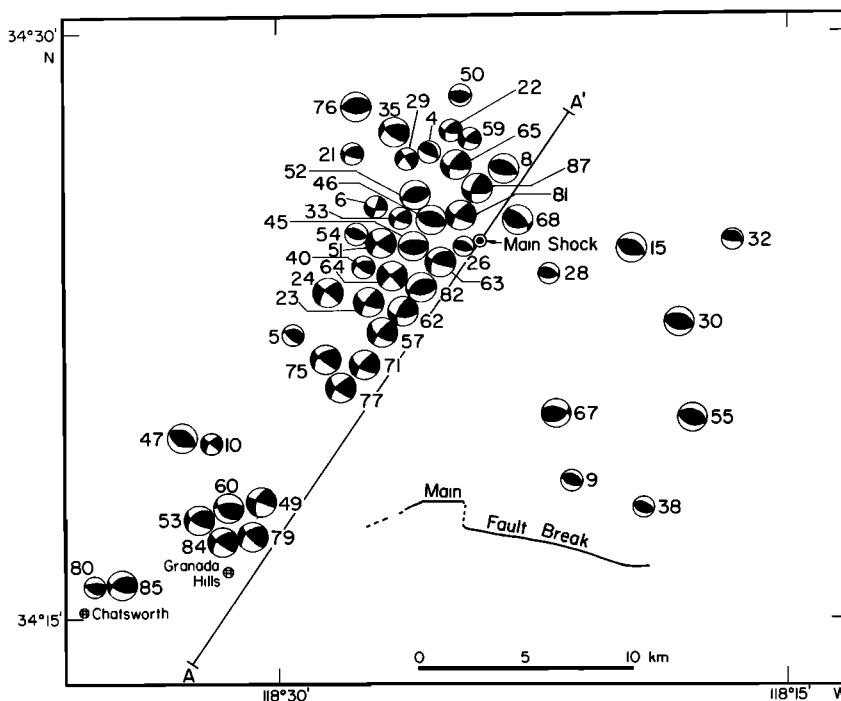
Fig. 9. Map of all A and B quality focal mechanisms that fit the model of Figure 8 (see legend of Figure 7). The epicenters may be slightly in error where the diagrams are crowded.

nary stages in the aftershock sequence (separated by the arrows in Figures 2c and 2d) are defined by the events that fit the fault model of Figure 8: the first 18 days during which thrusting activity extended east of A-A'; February 27 to about April 17, when activity was mostly confined to the west of A-A' (this stage, from evidence presented below, may have started 6 days earlier); and perhaps a third stage beyond April 17 when model-related activity east of A-A' is present again. This division also coincides with the overall distribution of aftershocks with time in Figure 2a. The first stage contains the initial surge of aftershocks defined by a rather sharp cutoff on February 26; the second stage is characterized by a burst of aftershock activity initiated by $M_L = 4.0$ or larger shocks (these series are discussed below); and the third stage is characterized by a low aftershock rate with few $M_L = 4.0$ or larger events.

It is difficult to compare the whole set of focal mechanisms with the model of Figure 8 by placing them all on a single map because they are too numerous. A more compact method of comparison is provided by the classic parameters of the double-couple focal mechanism: the two slip vectors, the compression axis, and the tension axis. The model predicts certain ranges of these parameters, which are shown in Figure 10; the approximate deviations from the ranges corresponding to the A quality (10° variation, shaded region) and B quality (20° variation, open region) focal mechanisms indicate the regions of expected scatter. The slip vector in the auxiliary plane, the compression axis, and the

Slip Vectors   Compression Axis   Tension Axis
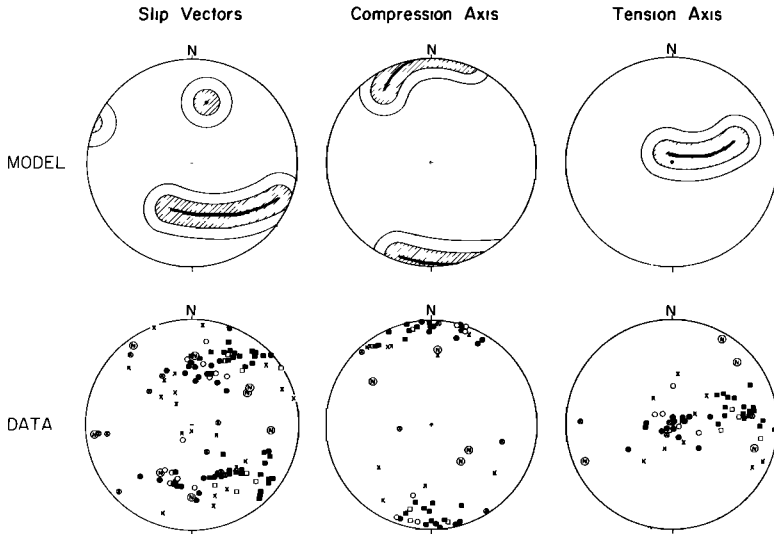
MODEL

DATA

Fig. 10. The classic focal mechanism parameters (slip vectors, compression
axis, and tension axis) on the lower focal hemisphere for the model of
Figure 8 and for the data consisting of all A and B quality focal mechanisms.
Symbols represent strike slip (squares) and thrust (circles) that agree with
the model and normal (N) and other mechanisms (×) that do not agree
with the model. (See also symbol identification in Figure 11.)

tension axis all sweep out extensive paths. The only fixed parameter is the
north-northeast slip vector in the fault plane. This results from the requirements
that the medium through which the fault surface passes be perfectly rigid and
that no voids be created along the surface. The data for all the A and B quality
focal mechanisms are shown in Figure 10 with symbols representing strike slip
and thrust that agree with the model and normal and other mechanisms that
do not agree with the model; the last two classifications are discussed below.
Focal mechanisms of A quality are indicated by either solid points or circled
letters. Most of the aftershocks fit the fault surface model of Figure 8 very
closely. The compression axes point generally north-south and nearly horizon-
tally, and the tension axes point between vertical and east, depending on whether
the mechanism is thrust or strike slip, respectively. The slip vectors in the
fault plane scatter a little more than expected; the strike slip data dip shallower
and point more easterly than those of the thrust mechanisms. Although it is
difficult to completely rule out some systematic bias introduced by the station
distribution or the focal mechanism fitting technique, this consistent deviation
between the thrust and strike slip fault plane slip vectors is considered real. As
will be seen below, it has some bearing on the idealistic assumptions of rigidity
and volume conservation used to formulate the initial model.

Precise locations of the aftershock hypocenters provide an important means
of testing the three-dimensional fault surface model, especially because of the
fault's complex nonplanar nature. Only A and B quality locations in conjunction
with A and B quality focal mechanisms are used, and these are presented in

map view in Figure 11. The symbols represent strike slip and thrust mechanisms that agree with the model and normal and other mechanisms, as in Figure 10. As identified earlier, there is a well-defined linear zone along and west of the line A-A′ containing a majority of the events. We now project all of the points west of A-A′ in Figure 11 onto a vertical plane along A-A′ and present the resulting cross section in Figure 12a. All the strike slip events south of the main event in this plot are limited to a shallow-dipping zone indicated by shading in the figure. Further, all but one thrust event, which is toward point A and is fairly distant from A-A′ (see Figure 11), plot below the strike slip zone. This is strong confirmation of the down step in the western portion of the fault surface model in Figure 8. The same cross section for those events east of A-A′ is shown in Figure 12b. The depths of these events are scattered but tend to plot above or in the upper part of the strike slip zone with only three exceptions, events 30, 48, and 55 (locations are shown in Figures 9 and 11). A further characteristic of the fault surface model is that the thrust mechanisms in the western limb of aftershocks should be not only deeper but farther west compared with the strike slip mechanisms. In Figure 13, we project all of the points of Figure 10 onto a plane perpendicular to the line A-A″ (shown in Figure 12a); this corresponds to viewing the fault surface nearly edge-on but at a somewhat shallower angle. It is immediately apparent that the thrust events to the left (northwest) of the main shock and A-A′ tend to be below and to the northwest of the strike slip zone, as the model predicts.
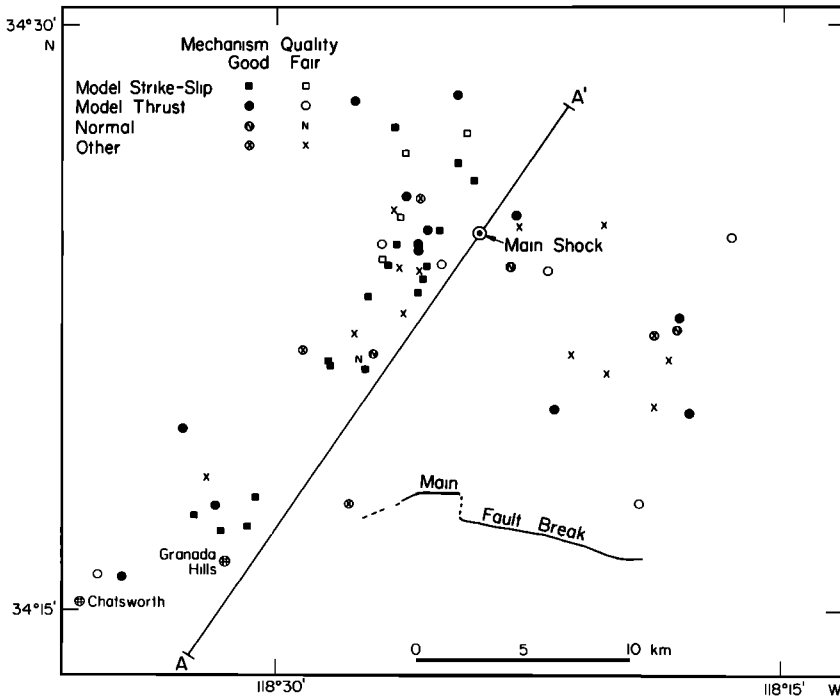
Fig. 11. Epicentral location of shocks with B or better quality for both locations and focal mechanisms.
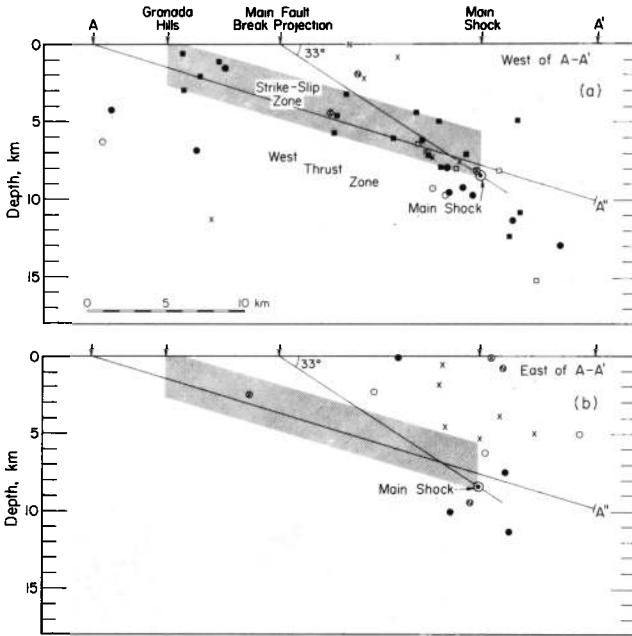
Fig. 12. Projection of hypocenters from Figure 11 onto the cross-section A-A' for (a) aftershocks west of A-A' and (b) aftershocks east of A-A'. The west thrust zone and strike slip zone shown in (a) correspond to the structure in the westerly part of the model in Figure 8.
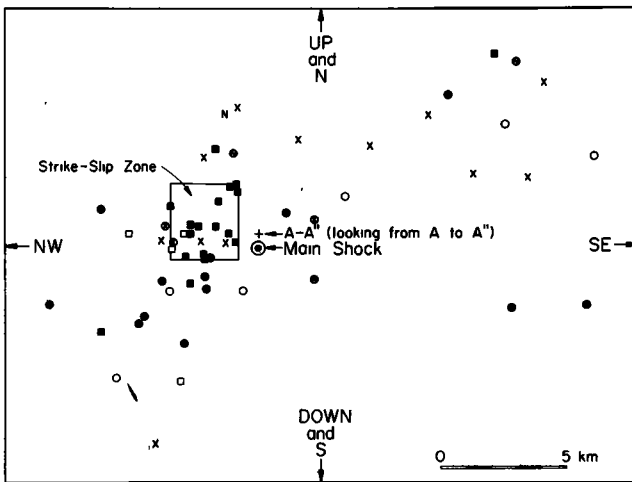

Fig. 13. Projection of hypocenters from Figure 11 onto a plane perpendicular to A-A'' (see Figure 12). Here the strike slip zone of Figure 12 is given a third dimension.

   As was noted previously, half of the focal mechanisms along the western
limb have a steeply dipping plane striking northeast nearly parallel to the limb
direction with left lateral strike slip motion (Figure 9). The model shown in
Figure 8 predicts that the strike of this plane should vary from a direction
exactly parallel to the limb direction (the direction of A-A') for a perfectly
vertical fault surface to a direction somewhat east of the A-A' azimuth for a
fault surface dipping steeply to the northwest. Northeast strikes of all the
strike slip events in the western limb are plotted in the azimuthal histogram of
Figure 14. The histogram interval is 5°, and the direction of A-A' is shown for
reference. The data have a well-defined peak just east of the direction of A-A'
and thus indicate consistency with the model.

   The hypocentral location of the main shock (Figure 12) is surprisingly
close to the aftershock distribution in light of its estimated location accuracy
(within 4 km horizontally and 8 km vertically). *Hanks* [1972], on the basis of
his analysis of the Pacoima Dam accelerogram and distant recordings of the
main shock, suggested a hypocentral depth of 12–15 km. But this would be in
the range of both the aftershock distribution and the calculated main shock
hypocenter if the latter is shifted down and to the northeast about 4 km, an
adjustment within the stated location accuracy. Thus the main shock depth
estimated by C. R. Allen et al. (unpublished data, 1972) and *Hanks* [1972] gen-
erally agree with the aftershock distribution and clearly show that the initial
rupture of the main thrust fault was near its lower, northernmost edge.

   c. Events that deviate from the model.   One-third (25/75) of the A and
B quality focal mechanisms do not fit the fault surface model of Figure 8. An
important subset of this group is composed of focal mechanisms that have normal
fault motion, that is, those for which the center of the equal-area projection falls
in the dilatational quadrant. Figure 15 presents all seven of the A and B quality
focal mechanisms that have normal fault motion. They are shown as a map
of schematic diagrams of the double-couple mechanisms. For these events the
tension axis is nearly horizontal, and the compression axis is shifted significantly
from its usual north-south, nearly horizontal configuration. This is seen in the
data for the normal mechanisms designated as *N* in Figure 10. Three of the
normal events are scattered in the eastern aftershock region, one is near the main
shock epicenter, and a clustered group of three centers is on the line A-A' in
the central portion of the west aftershock limb. The cross sections in Figure 12*a*
and 12*b* (again, these include only A and B locations) show that the scattered
normal events in the eastern region are shallow; the event near the main shock
epicenter is deep, possibly owing to a bad location computation, and the group

Fig. 14. Radial histogram in 5° intervals of fault
plane strikes for all strike slip events in the western
aftershock limb. The model of Figure 8 predicts that
the strikes would group slightly to the east of the
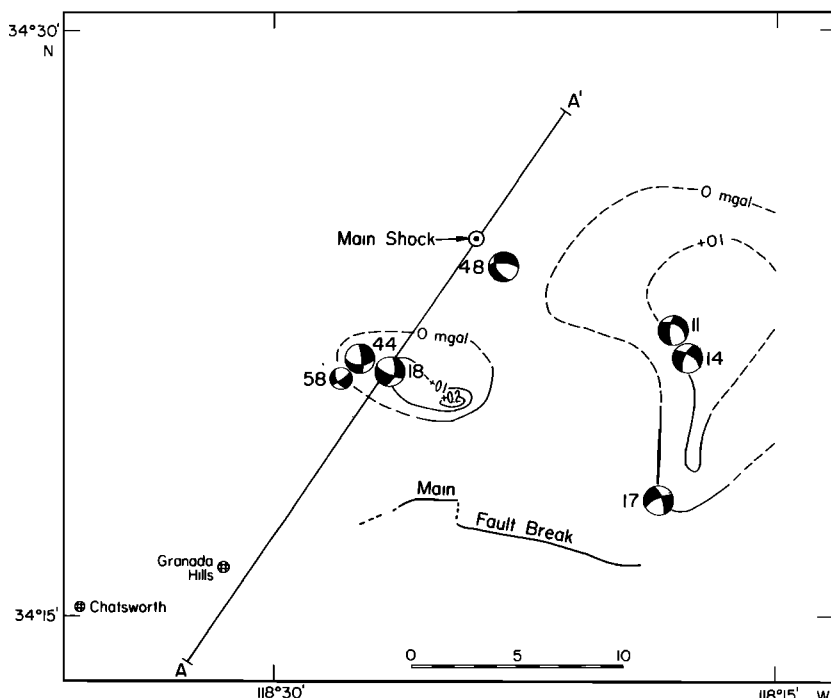direction of A-A', as the data confirm.
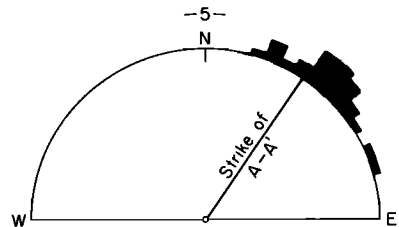
Fig. 15. Map of focal mechanisms of the normal group (see the legend for Figure 7). Their locations correspond well with areas of shallow tensional stress associated with ground subsidence that is indicated by the outlined areas of positive gravitational acceleration change [*Oliver et al.*, 1973]. Negative changes are not shown.

straddling A-A' is shallow. The shallow depth and association with the upper thrust block of all but perhaps the normal event near the main shock agree with effects due to curvature of the main fault surface, as is discussed below. However, the tight clustering of normal events along the edge A-A' of the strike slip zone indicates that other stress disturbances may play a role in these three events. A clue for such an inhomogeneous stress in this region has already been provided by the discrepancy of fault plane slip vectors in Figure 10 between strike slip and thrust events. If, as the slip vector data indicate, the upper block's southerly motion is more to the west in the strike slip zone than that to the east of A-A', then the motion would tend to create a void along the main fault's down step that would manifest itself as extension in an elastic material.

Exceptionally good confirmation of the areas of compressional release is seen in *Oliver et al.* [1973, Figure 3]. Their data, which show the change in gravitational acceleration due to the tectonic motions of the San Fernando series, outline two areas of acceleration increase; this implies a decrease in the ground elevation that results from local compressional release. The areas of positive acceleration change [after *Oliver et al.*, 1973] are outlined in the map of the normal events in Figure 15. One area, relatively confined in lateral extent,

coincides with the location of the three normal events along the central west aftershock limb. A second, much broader area coincides with the normal events in the eastern aftershock area.

A histogram showing the time sequence of the normal events is shown in Figure 2e. If the larger set of aftershocks is a fair representation of the aftershock activity, we must conclude that events with normal faulting cease after only 10 days (February 29) into the aftershock sequence. One might fairly inquire as to the statistical significance of this distribution. This can be easily estimated by assuming that the normal events are randomly distributed throughout the set and calculating the joint probability that they would all occur before February 19. The probability is 4%, which indicates that the observed lack of normal events after February 19 is significant. Thus, no matter what their source, the tensional stresses causing the normal events seem to be compensated within a time period of about 10 days. This falls within and further characterizes the first stage of the series defined earlier.

The remaining 18 events that do not fit the fault surface model are shown in the map of schematic focal mechanisms in Figure 16. A commonly occurring focal mechanism type in this set can be classified as northeast striking thrust faults. The events of this type which fall near the strike slip zone, events 61, 66, 76, 73, 74, 78, and 83, can be explained by southeasterly thrust motion on the fault surface model of Figure 8. This motion is consistent with the idea of compensation for the deviatory tectonic movements causing tension and normal
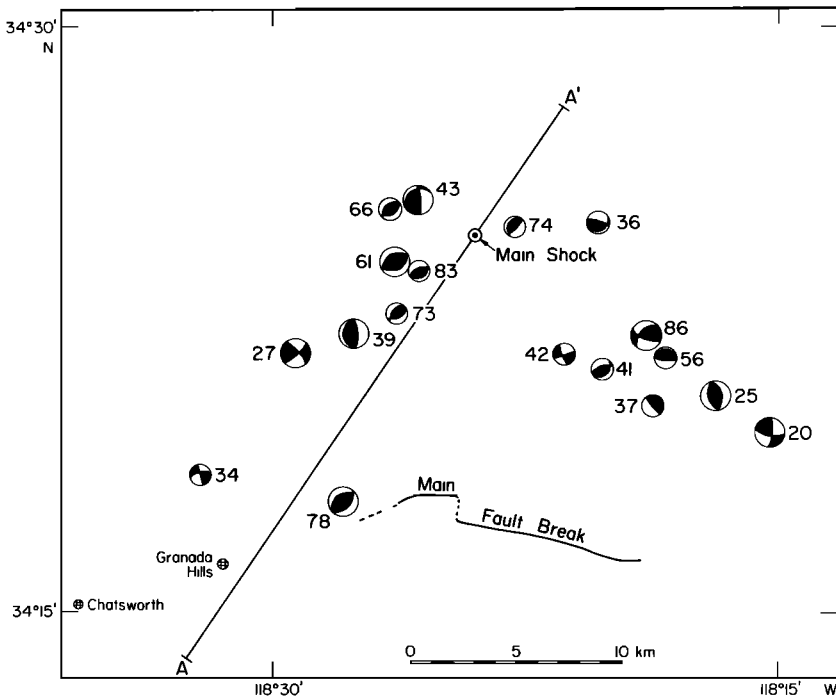

Fig. 16. Map of focal mechanisms of the other group (see the legend for Figure 7).

events along A-A'. Support for this hypothesis comes from the fact that the last normal event occurred in the central west limb vicinity along A-A' on February 19 (event 58), and the first compensatory thrust event described above occurred on February 21 (event 61), less than three days later. Thus this time would mark the initiation of a north or northwest compressional addition to the local stress in the strike slip zone that stops the shallow normal events and even causes a series of compensatory southeasterly thrust movements on the main down-stepped fault surface. As can be seen in Figure 2a, February 21 also stands out as the first day after February 10 that had events of $M_L = 4.0$ or larger, initiating the series of events 61–64, which closely concentrate in the northern part of the west limb.

If the compensatory thrust events, which begin on February 21, are separated from the events on Figure 16, we find that, remarkably, all but one of the remaining events occur in the first stage between February 9 and 17, as shown in the histogram of Figure 2f. The exception occurred late in this set on April 25 during the possible third stage, which was indicated above. Most of these events are in the upper thrust block east of A-A' (see Figures 16 and 12b). From these considerations, we conclude that these remaining events represent complex fracturing in the upper thrust block resulting from the main tectonic motion. Their activity ceased at the same time, and probably for the same reason, as that of the normal events near February 19–21, and may have been reinitiated near the latter part of April.

d. *The dip of the main thrust fault.* As seen from the *P* wave first motions of the main shock shown in Figure 5, the dip of the fault at the initial rupture point is well determined at about 52°. But a line from the main surface rupture to the hypocenter of the main shock computed at 8.4 km depth by Allen et al. (unpublished data, 1972) dips at only about 33° (Figure 12a shows an approximation of the dip line). Also, the fault plane slip vector data in Figure 10 indicate an average plunge of around 40°, although the strike slip event slip vectors plunge shallower and trend more to the east than those of the thrust events.

Additional evidence for steepening of the fault plane to the north is presented by the cross section of Figure 12a. There is a notable steepening of the hypocentral distribution of strike slip events to the north in the zone of the main shock's hypocenter. Because of the seismometer station distribution, this region gives the best control for hypocentral determinations, and therefore the steepening is probably real. Note that the thrust hypocenters in this zone can be accounted for in the existing model of Figure 8 without modification, and only the three deep strike slip events to the north indicate steepening.

Most of the events that are near the hypocenter of the main shock are west of A-A' (see Figure 11). Thus the slip vectors of the model-compatible events along the west limb should provide a good test to show a systematic steepening to the north. Figure 17 is a plot of the slip vector plunge as a function of distance along A-A' for these events. Some increase of plunge to the north can be seen, especially if only the strike slip events (square symbols) are considered. But the steep plunge of slip vectors from the thrust events in the southwest area (toward A) conflict with this interpretation unless the fault surface also includes a steep-

ening in the extreme southwestern portion. The main characteristic of the data in Figure 17 is that the slip vectors of strike slip events plunge less than those of the thrust events. The thrust events in turn have plunges that are not significantly different from the range of the main shock (a range is shown because of the uncertainty of the main shock's auxiliary plane determination). East of A-A', the fault plane slip vectors of thrust events are also not significantly different from that of the main shock and show no systematic steepening to the north (see Figure 9). One possibility that would reduce the steep thrust fault dips is a change of the hypocentral velocity used to calculate the focal mechanisms, especially that of the main shock. An increase in P wave velocity of about 0.8 km/sec (from 6.1 to 6.9) would have the effect of shallowing the thrust plane dip of the main shock focal mechanism (from about 50° to about 40°). This velocity is not totally unrealistic for certain crustal rocks, but no evidence exists for a velocity this high at the main shock's hypocenter.

Although it is apparent from the discussion above that the evidence is not conclusive, we believe that the arguments in favor of the fault steepening with depth are stronger. Thus we support the early results of many investigators [Hanks et al., 1971; Wesson et al., 1971; Wesson and Wilson, 1972; C. R. Allen et al., unpublished data, 1972) that the main thrust fault surface dips at 35°–40° near the surface and steepens to 52° at the main shock hypocentral depth, 8–12 km. Wesson and Wilson [1972] used this conclusion in their proposal that the San Gabriel fault was the main rupture surface at depth; we discuss this possibility in a later section.

    e. Early March and March–April series. During what is defined as the second stage of the overall aftershock series, at least two significant bursts of
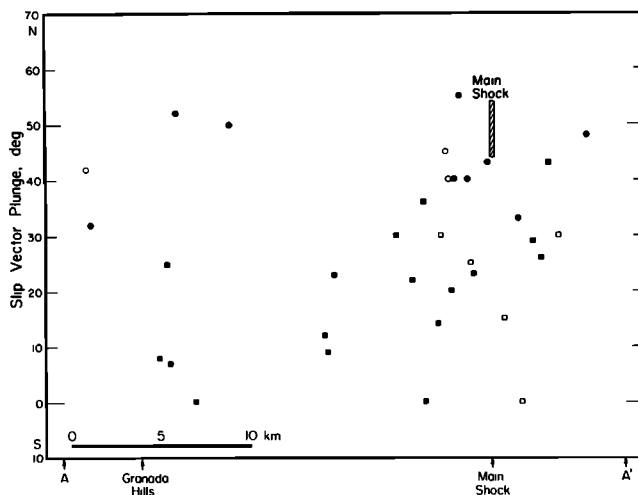

Fig. 17. Slip vector plunges for all events west of A-A' (see Figure 11) as a function of distance along A-A'. Squares are strike slip events, and circles are thrust events. Steepening to the north is indicated if the thrust events near A can be ignored.

activity occurred in the set of events larger than $M_L = 3.0$. The first series began on March 7 with an $M_L = 4.5$ event in the central portion of the west limb. Three events followed on the same day and all were in or near (within 1.5 km) the west limb. The activity for several days both before and after the series was less than an event per day, as is seen in Figure 2b. The second series began 18 days later on March 25 with an $M_L = 4.2$ event at nearly the identical hypocenter as the initial event of the first series. Eleven events followed over the next 8 days, and all were also in or near (within 2.0 km) the west limb. Five of the aftershocks in this series had M_L of 4.0 or larger, and one, on March 31, caused some further damage in the Granada Hills area. No intervening events above $M_L = 3.0$ occurred in the time between the two series, and the average activity of events this size was less than 1/day after the end of the March 25 series.

The parallelism between the two series is striking: initiation at the same location by shocks of $M_L = 4.0$ or larger, relative quiescence both before and after each series, and a limitation of epicenters to the west limb. But even more significant is the time sequence of the series' events along the west limb. Figure 18 is a plot of the event times as a function of distance along A-A' (see Figure 11). The symbols again represent the focal mechanism types, and the adjacent set of numbers indicates the event numbers and M_L values. Blank spaces indicate aftershocks larger than $M_L = 3.0$ that are not in Table 1 whose hypocentral locations should be considered of C quality. Lines connect events that are adjacent in time, and are dashed where one of the events is not in Table 1. The data show a systematic sequencing of aftershocks along the west limb, especially when several events occur advancing in one direction along the limb, such as the sequences 71–74 and 76–80. On the basis of this sequencing in two separate aftershock series that have other strong similarities, we conclude that the time-space distribution of both series is not random, and therefore a causal relationship must exist between the events within each series. This causal relationship may not be as simple as that implied by connecting successive events with lines as in Figure 18. However, where several events occur sequentially in one direction of advance, as in the previously mentioned sequences 71–74 and 76–80, a propagating phenomenon that triggers events with an apparent horizontal velocity of 4–15 km/day is suggested. It is interesting to compare these rates with rates of 0.5–10 km/day observed for propagating creep events in Central California (Robert Nason, personal communication, 1972). The slopes corresponding to these velocities are shown in Figure 18. The propagation rates of the aftershocks in Figure 18 are at the higher range of the rates observed by Nason, but they are certainly comparable.

   f. Regional tectonics and seismicity. Figure 19 outlines most of the major faults in an area from Santa Monica Bay on the southwest to the Mojave desert on the northeast [modified from *Jennings and Strand*, 1969]. The approximate area of the aftershock epicenters is shown for reference. The San Fernando fault trace occurs in the southeastern edge of the Ventura basin, a highly folded synclinorium within the Transverse range province that contains remarkably thick sections of Tertiary and Quaternary strata (up to 6 km in the Santa Susana mountains area [*Wesson and Gibbs*, 1971]). The basin contains many
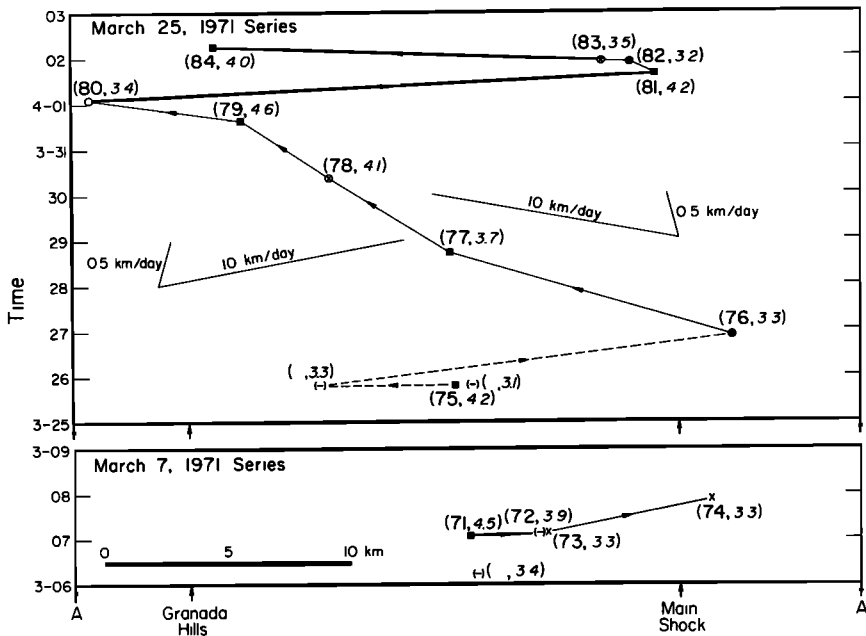
Fig. 18. Aftershock origin time as function of distance along A-A′ (see Figure 10) for all events larger than $M_L = 3.0$ during March 7-8, 1971, and March 25-April 2, 1971. The larger numbers correspond to those of the events in Table 1 (events not in the table have no numbers) and the smaller numbers to the magnitudes. The symbols are described in Figure 11 except for the dashes, which indicate events with no focal mechanism.

thrust faults on which much of the uplift of the adjacent mountains has taken place. Of these thrusts, the Santa Susana fault, which shows evidence of late Quaternary movements [Wentworth et al., 1971], is the closest to the San Fernando fault and lies immediately to the west, as is seen in Figure 19. Oil field data on the western and eastern part of the Santa Susana thrust show that it has a shallow north dip at the surface and steepens to about 50° when it reaches 0.7-km depth [Hall et al., 1958; Roth and Sullwold, 1958]. Similar oil field data on the San Cayetano thrust farther to the west (not shown in Figure 19) indicate a 30°-35° north dip at the surface steepening to about 50° as it reaches depths near 4 km, as shown in Figure 20 [Bailey and Jahns, 1954]. This is precisely the dip behavior proposed for the San Fernando thrust fault, which is part of the same fault system.

Of further interest in the San Cayetano thrust area are the mapped normal dip slip faults dipping to the north in the upthrust block just north of the San Cayetano fault trace. This faulting is also in agreement with the San Fernando fault tectonics, specifically the focal mechanisms and gravity data in the northeast aftershock zone, which indicate shallow normal faults (Figure 15).

The theoretical and experimental work of Sanford [1959] directly bears on the phenomena of thrust faults steepening to dips greater than 45° with depth and the occurrence of shallow normal dip slip faults in the upthrust block. San-
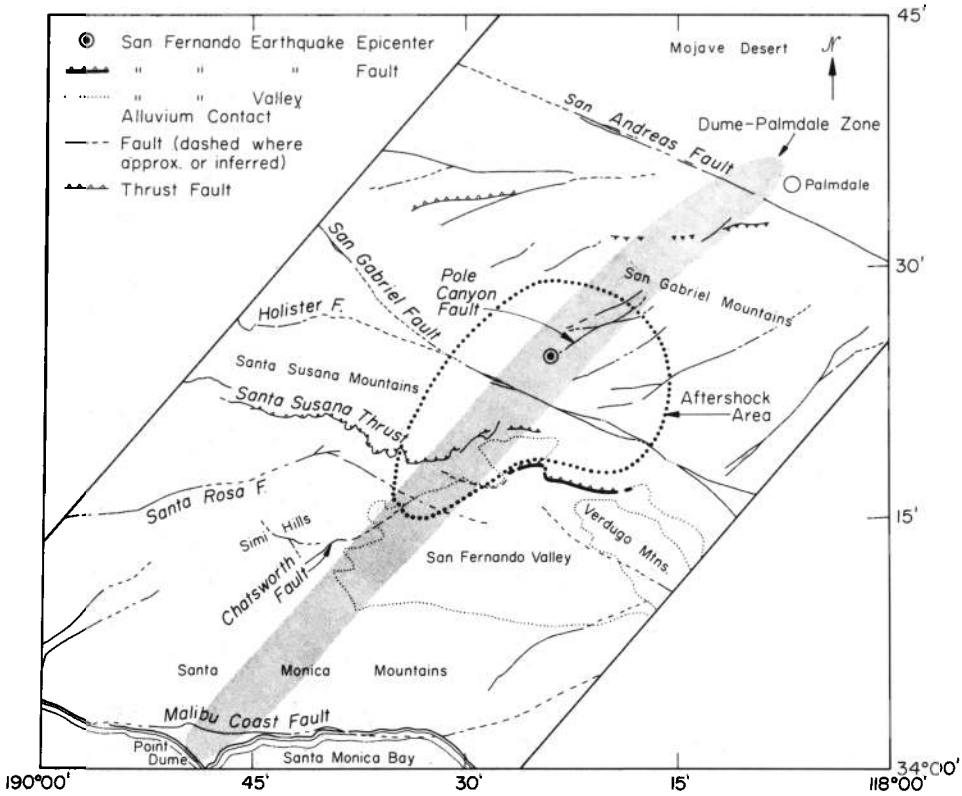
Fig. 19.   Major tectonic features in the area around San Fernando.

ford showed that the normal faulting is a result of the steepening of the thrust
fault and that the steepening itself is directly related to laterally varying vertical
forces at depth. The steepening can be simply explained by the fact that all
vertical forces at depth must converge to zero at the earth's surface. Thus,
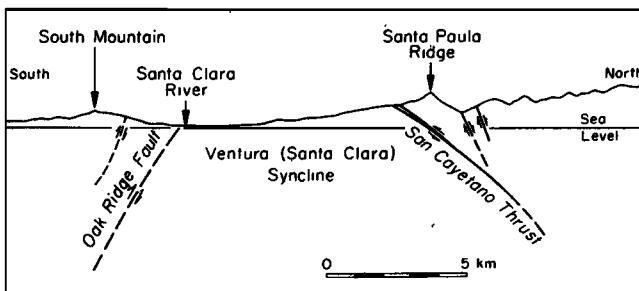although laterally varying vertical forces can be supported by rock strength at

Fig. 20. Cross section of the Ventura syncline showing the
San Cayetano thrust fault [modified from *Bailey and Jahns*,
1954, Figure 8]. Note the steepening with depth and the normal
faulting to the north.

depth and cause fractures dipping steeper than 45°, the only possible stresses at the earth's surface are horizontal, and fracture criteria require a thrust fault that dips shallower than 45°. Sanford's results are shown in Figure 21.

The implications of these laterally varying vertical forces are important to the regional stress picture. Emphasis in the vicinity of the San Andreas fault is commonly placed on horizontal movements and stresses dominating the tectonics, especially since the emergence of concepts of plate tectonics. However, it is clear from the above that significant vertical stresses other than overburden pressure are also acting at depth in the Ventura basin. The question naturally arises as to the relative magnitude and origin of these stresses. First, the horizontal stresses must be a substantial part of the regional stress field because the extensive folding in the Ventura basin is due to north-south compression [Bailey and Jahns, 1954], which is still active. Isostatic imbalance is not the cause for the vertical stresses because it is apparent that the mountains north of the Ventura basin have been moving up, and this would require a mass deficiency under the mountains. But seismic and gravity evidence for the San Gabriel mountains, which were uplifted in the San Fernando earthquake, indicate no mass deficiency and perhaps even indicate an excess [Mellman, 1972]. It appears that the most likely cause for the vertical stresses is a partial upward redirection of the horizontal stress, either by a deep obstruction over which the surface blocks are forced or by complex distortion due to buckling at depth as the crust is shortened. Indeed, the great bend in the San Andreas fault zone as it crosses the Transverse ranges of southern California virtually demands vertical adjustments in the adjacent regions if lateral movements are to be continuous along the San Andreas fault. The stress at depth in the Ventura basin area is most likely a combination of a dominant horizontal stress and laterally varying vertical stress, as in Sanford's model, that would result in the major compressional stress axis dipping 10° or more at depth.

The existence of the left lateral strike slip zone, which is the down step in the fault surface model of Figure 8, is well established from the focal mechanisms and the southerly curvature of the aftershock zone and main fault break in this region. As was pointed out by Allen et al. (unpublished data, 1972), further support for the existence of the down step comes from the mapped geology of the area [Wentworth et al., 1971, Figure 2]. The trace of the Santa Susana thrust makes a sharp bend to the north when it enters the zone from the west (Figure 19) in exactly the manner postulated for the San Fernando fault. Further, basement rocks are widely exposed in the San Gabriel mountains east of this zone, whereas only younger sedimentary rocks are exposed to the west. The latter fact strongly supports the concept of a flexural or faulted down step to the west in this area. However, it is not clear that the thrust faulting to the west of the zone is associated with a single down-stepped thrust fault, as depicted in the model of Figure 8, or as two or more parallel thrust faults for which there are several

Fig. 21. Results of an experimental fracturing experiment by Sanford [1959, Figure 17] that shows a thrust fault steepening with depth and tensional fractures in the upthrust block.
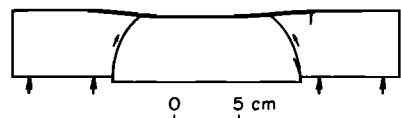
candidates in the mapped geology of the area [*Jennings and Strand*, 1969]. The
western thrust mechanisms occur mainly in the extreme northwest or southwest
corners of the aftershock zone, with only one intervening thrust event (event 5)
in the central part of the zone (Figure 9). Also, the steep slip vector plunges of
thrust events near Granada Hills (Figure 17) and deeper hypocenters (Figure
12a) deviate from the model and the hypothesis of a shallow fault dip at the
surface; however, these effects may be related to the greater hypocentral location
inaccuracies in this region. Although these are not serious objections to this
feature of the model, they point out the possibility of more than one thrust sur-
face extending to the west of the established main fault down step.

The San Gabriel fault is a major structural feature in the San Fernando area,
and its trace cuts through the center of the aftershock zone (Figure 19). Although
it has some evidence of dip slip, its main motion has been right lateral strike slip,
with no evidence of late Quaternary displacements [*Wentworth et al.*, 1971].
Dip measurements of the San Gabriel fault in the aftershock region are com-
plicated in many locations by nearby parallel thrust faulting that cuts across
the San Gabriel fault plane. But where the fault is uncomplicated and clearly
exposed, it is steeply north-dipping at 70° to 80° [*Oakeshott*, 1954, also personal
communication, 1972]. This steep dip agrees with the extreme linearity of the
fault trace as it cuts through the varying topography of the western San Gabriel
mountains. *Wesson and Wilson* [1972] have proposed that the San Gabriel fault
was the initial rupture surface of the San Fernando earthquake. They based this
on the steepening with depth of the San Fernando fault surface and on ground
elevation changes in the vicinity of the San Gabriel fault trace. As was discussed
above, evidence seems to favor a steepening of the San Fernando thrust fault
surface with depth, but this is a characteristic of all the north-dipping thrust
faults along the Ventura basin. It is more likely that the steepening of the San
Fernando fault is due to the same cause and not to its special geometrical relation-
ship with the San Gabriel fault, which appears to have a very different geologic
history. Also, as is stated above, the dip of the San Gabriel fault is probably
steeper than 52°, the dip of the initial San Fernando rupture surface. The positive
gravity changes in the northeast aftershock zone shown in Figure 15 indicate
that the ground surface just north of the San Gabriel fault experienced a decrease
in elevation. If any shallow displacements took place on the San Gabriel fault,
this evidence indicates that it was normal dip slip instead of thrust.

Seismicity in the region of Figure 19 before 1971 shows some interesting
earthquake distributions. Figure 22 is a map of epicenters for all events located
by CIT for the time periods 1961–1962 (Figure 22a), 1969 (Figure 22b), and
1960–1970 (Figure 22c). The locations are believed to be accurate to within
about 9 km. The San Fernando aftershock zone and some of the major faults
are shown for reference. During 1961–1962 (Figure 22a), the earthquakes clearly
define a zone that coincides with the location and direction of the west limb of
San Fernando aftershocks but extends from Point Dume near Malibu on the
southwest to the San Andreas fault near Palmdale on the northeast. For dis-
cussion purposes it will be designated the 'Dume-Palmdale zone,' and it is out-
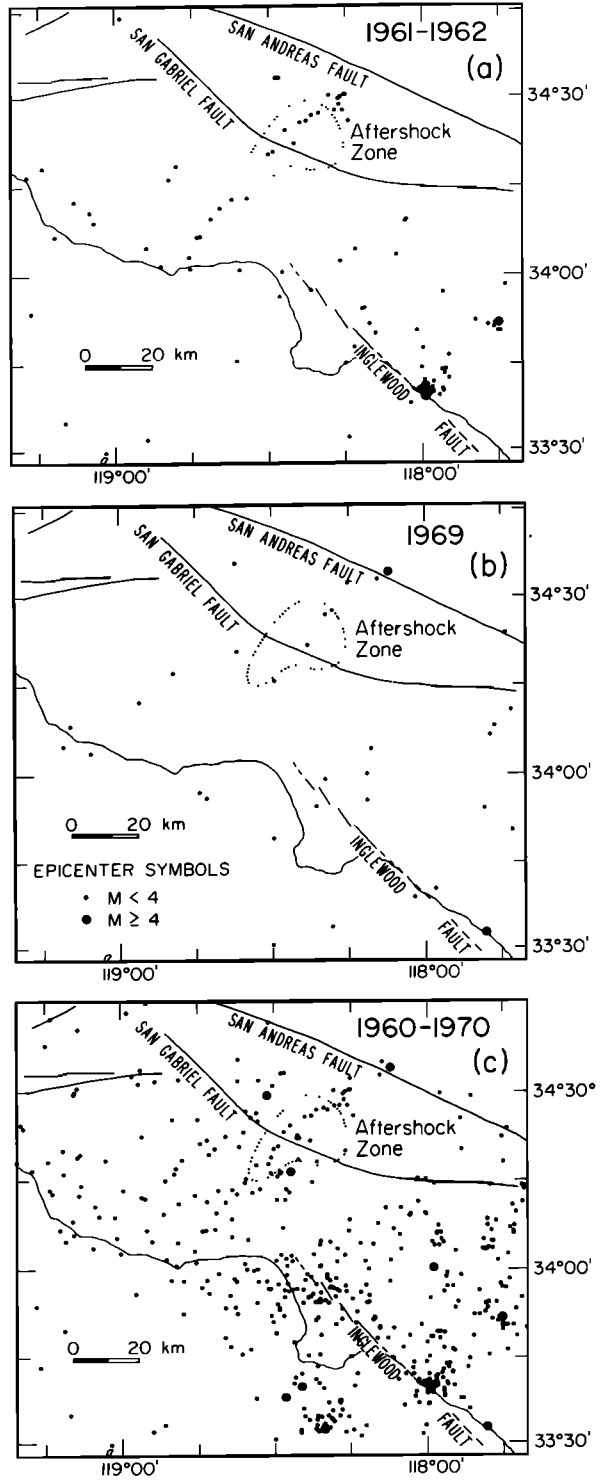lined in Figure 19. Figure 22b shows that the northeastern part of this zone was

Fig. 22. Seismicity around the San Fernando region for the time periods (a) 1961–1962, (b) 1969, and (c) 1960–1970. The epicentral locations are believed to be accurate to within 9 km. The San Fernando aftershock zone and some of the major faults are shown for reference.

active in 1969 and included an $M_L = 4.0$ event on the San Andreas fault. Figure 22c confirms that the Dume-Palmdale zone is suggestively outlined even when compared with the total seismicity over the 10-year period before the main shock, 1960–1970. No similar pattern in the zone is seen in the years prior to this interval back through 1935, although this may be because the earlier epicentral locations are considerably less accurate. There is a possible indication of activity along the zone from the $M_L = 5.2$ earthquake of August 30, 1930 [*Wentworth et al.*, 1971]. The original epicentral assignment, which was not well constrained, was in the Santa Monica Bay. But, minor damage at both the Chatsworth Dam and Lower Van Norman Dam, which lie along the western edge of the San Fernando Valley, suggests that the epicenter was on or near the Dume-Palmdale zone. Other lineations that are outlined by seismicity but do not coincide with any obvious surface structure in Southern California are reported by *Ryall et al.* [1966] and *Richter* [1969]. These lineations often strike in the direction nearly perpendicular to the major northwest-southeast strike slip faults of the region; this is approximately the conjugate shear direction in association with a dominant horizontal compression.

The significance of activity on the Dume-Palmdale zone is that it precedes the San Fernando series and exactly coincides with the west aftershock limb and the main shock epicenter as seen in Figure 19. Although the zone is not obviously outlined by continuous geologic features of the area, there are some mapped structures that appear to be related. The sharp bend in the trace of the Santa Susana thrust has already been mentioned. The western edge of the San Fernando Valley also lies along this trend and is fault controlled with the east side down [*Corbato*, 1963]. One of the members of this family of faults is the Chatsworth fault, which shows some evidence of Quaternary displacements [*Wentworth et al.*, 1971]. Although some maps show the northwest-trending Northridge Hills fault as cutting continuously across this zone, geologic relationships in the area of intersection are obscure. Still farther south, however, the Santa Monica mountains and the Malibu coast fault are clearly continuous across the Dume-Palmdale trend, and the zone must terminate in this area.

North of the San Gabriel fault, parallel to and within the Dume-Palmdale zone, are a number of northeast-trending faults that have had a history of left lateral displacement. For example, *Oakeshott* [1958] points out that the east-trending Soledad fault is clearly offset by the northeast-trending Pole canyon fault, which passes virtually through the epicenter of the San Fernando earthquake. However, most of these faults seem to have been active primarily in Miocene time, with no major displacements since that time (L. T. Silver, personal communication, 1972). This represents a major problem, because the San Gabriel fault itself appears to have had about 50 km of right lateral displacement in Pliocene-Pleistocene time [*Crowell*, 1952, 1962, p. 39] and thus it should have displaced these earlier northeast-trending faults. If one accepts the large movement on the San Gabriel fault, he cannot argue for a continuous Dume-Palmdale zone that has been active since Miocene time. There are, however, many northeast-trending faults within the Transverse ranges north of the San Gabriel fault, and it is not necessary to assume that the faults currently delineating the Dume-Palmdale zone have always been in their same relative positions.

Regardless of the complex geologic history of the region, the Dume-Palmdale zone appears to be an active zone at the present time, perhaps taking advantage of previously existing lines of weakness. The location of the San Fernando main shock, the strike slip zone of the main fault surface, and the seismicity represented in Figure 22 currently show the zone to be a linear region of weakness where stress can be concentrated. This leads us to believe that the zone represents a decoupling boundary between crustal blocks that permits them to deform separately in the prevalent crustal shortening mode of the region. The fact that this zone of weakness does not extend northeast across the San Andreas fault is evidence that it is being carried along in the crust or lithosphere as displacement takes place along the San Andreas. Apparently, most of the crustal shortening is done south of the San Andreas in this area, as is reflected in the aseismicity of the Mojave block to the north [Allen et al., 1965]. The aseismicity is probably related to greater strength in the Mojave block due to its thicker crust [Mellman, 1972].

6. SUMMARY AND CONCLUSIONS

The main shock of the San Fernando earthquake occurred at 14h 00m 41.8s UT on February 9, 1971. C. R. Allen et al. (unpublished data, 1972) assigned it a magnitude M_L of 6.4 and a location at 34°24.7′N, 118°24.0′W, $h = 8.4$ km; they estimated the hypocenter to be within 4 km horizontally and 8 km vertically. Hanks [1972], on the basis of his analysis of the Pacoima Dam accelerogram and distant recordings of the main shock, suggested a hypocentral depth of 12–15 km, which is within the range given by Allen et al. A main shock depth of 12 km is compatible with the location of the aftershocks of Figure 12 if the epicenter is shifted northwest about 4 km, again within the range given by Allen et al. Thus, within the constraints of the data, the location of the main shock's initial rupture coincides with the lower, northernmost edge of the aftershock distribution.

The best focal mechanism fit to the P wave first motions of the main shock gives the initial thrust plane parameters: strike, N67°(±6°)W; dip, 52°(±2°)NE; rake, 72° (67°–95°) left lateral. Evidence from the slip vectors of the aftershocks suggests that the rake is closer to 80°, but this assumes that the main shock and aftershock motions were the same. The evidence of fault surface displacement from Kamb et al. [1971, Figure 2] scatters between the extremes of the rake angle.

To have as homogeneous a representation of the aftershock tectonics during the first three months as possible, the aftershocks were chosen for analysis on the basis of size. The first set of events were defined as all those of $M_L = 4.0$ or larger; 20 of these had onsets clear enough for analysis during the first three months of the series. The second set was defined as events with clear onsets at most of the CIT telemetered stations; this essentially corresponds to a magnitude cutoff at about $M_L = 3.3$, and a total of 87 aftershocks fulfilled the requirement. The second set, of course, contains the first. Of the second set of 87, only 12 focal mechanism solutions were poorly constrained, and most of these occurred during the first few hours of the series, when the portable stations were not yet in operation.

In both sets of aftershocks, most of the activity was along a linear northeast striking region encompassing the main shock epicenter and bounding the aftershock region to the west. This region, the west aftershock limb, is dominated in both aftershock sets by focal mechanisms in which one plane strikes along the limb and dips steeply to the northwest with left lateral strike slip motion. Thrust mechanisms resembling that of the main shock occurred both to the west and to the east of the west limb. From these considerations it is clear that the west limb outlines a major discontinuity in the main thrust fault surface. These data require a single nonplanar fault surface that incorporates a down step to the west in the north-dipping thrust fault plane, as shown in Figure 8. Two-thirds of the focal mechanisms are either strike slip or thrust with orientations and epicentral locations in agreement with the fault surface model, and they provide strong support for its validity. An interesting way of illustrating this is the comparison (shown in Figure 10) of slip vectors, tension axes, and compression axes of the focal mechanisms with the distribution of these parameters predicted by the fault surface model. Except for some scatter and minor deviations (which correlate with other phenomena in the series), the data clearly have the same distribution. Further confirmation for the model is provided by the agreement of fault plane strikes for shocks with strike slip mechanisms with the strike predicted from the orientation of the west aftershock limb. The hypocentral locations bear out the model's characteristics that the strike slip events along the west aftershock limb are limited to a narrow zone, at least south of the main shock epicenter, and that the thrusts in and to the west of the west limb tend to be deeper.

Although the dip of the main shock initial rupture surface is 52° (±2°), evidence from the main shock hypocenter relative to the surface faulting and the distribution of the aftershock hypocenters south of the main shock indicates a dip of around 35° at shallower depths on the main fault surface. There is also some indication of steepening with depth of the aftershock slip vectors, although this is not as clear. The complication arises from the thrust event slip vectors west of the west aftershock limb and may indicate that the thrusting to the west is not on a single down-stepped surface but is on two or more unconnected thrust planes. However, within and to the east of the west aftershock limb, the data favor a fault surface whose slip vector starts with a 50° plunge at the initial rupture at depth and curves to a 35° plunge as it extends to shallower depths.

A series of north-dipping thrust faults to the west of the San Fernando area exhibit steepening with depth in precisely the same manner as that proposed for the San Fernando fault. These faults strike along the trend of the Ventura basin and have late Quaternary movements that form mountains to the north in the same tectonic setting as the San Fernando fault. Sanford [1959] showed that this steepening to dips greater than 45° may be related to laterally varying vertical forces at depth, which has important implications to the regional stress picture. The most likely cause for the vertical stresses is a partial upward redirection of the horizontal compressive stress, which from the time of extensive folding in the Ventura basin to the present has been the dominant stress in the region.

The San Gabriel fault, a major structural feature cutting through the aftershock region, apparently played no significant role in the displacements of the

main San Fernando event. There is no evidence for late Quaternary displacements on the fault and no direct evidence that it slipped in the main event. At depth it is probably much steeper than the 52° dip of the initial rupture surface. Gravity data, which reflect ground surface displacements, indicate that, if any shallow displacements took place on the San Gabriel fault, they had a normal dip slip component.

One-third of the focal mechanisms do not fit the fault surface model of Figure 8. This is not surprising because the strain release due to the aftershocks is minor compared with that of the main shock, and some of the aftershocks should represent a relief of complex stress concentrations due to motions of the main shock. According to the theoretical and experimental work of *Sanford* [1959], one of these stress concentrations should be a tension field in the shallow upper thrust block resulting from the steepening of the thrust fault with depth. Ground surface elevation decreases and shallow normal focal mechanisms north of the main fault break confirm the existence of this tension field after the main event. A close concentration of shallow focal mechanisms and localized ground subsidence on the west aftershock limb near the western projection of the main fault break indicates further complexity. The consistent deviation between the strike slip and thrust event slip vector azimuths (Figure 10) predicts a divergence of motion along the down step of the west aftershock limb. This divergence, which would produce a local tension field, would be most pronounced as the down step of the main fault surface approaches the ground surface, which is the precise location of the observed concentration of shallow normal events and ground subsidence.

Another class of focal mechanisms can be separated from the events that do not fit the model. They are defined as events that occur along the west aftershock limb with a thrust plane striking in the same direction as the limb. The motion of these events is consistent with the idea of compensation on the down step fault surface for the divergence that caused local tension along the west limb. These compensatory thrust events did not begin until February 21, twelve days after the main shock. All the remaining focal mechanisms in this set were located in the upper thrust block east of the west aftershock limb and were confined with only one exception to the time period of February 9–17, before the onset of the compensatory thrust events. They are presumably related to localized stress concentrations due to displacements of the main shock.

Other evidence points to this time as one of significant change in the stress field of the aftershock area. The last normal focal mechanism in the set occurred on February 19, three days before the first compensatory thrust event. February 21 was the first day since February 10 that an event with $M_L = 4.0$ or larger occurred in the series; this initiated a series of aftershocks that closely concentrated in the northern part of the west aftershock limb. After this time, at least until April 17, the aftershock activity was characterized by isolated bursts of events starting with $M_L = 4.0$ or larger events. These bursts were essentially confined to the west aftershock limb until April 17, when the bursts ceased and minor activity continued throughout the aftershock area. The time-space distribution of these events indicates that some time near February 21, twelve days after

the main shock, a horizontal compressional stress in a north or north-northwest direction was added to the stress in the aftershock area. As a result, events related to stress release of the main shock ceased, and activity was concentrated in bursts of events along the down step of the main fault surface. Effects due to this change of stress appear to have stopped by April 17, about two months later.

While the aftershock activity was by no means finished after May 7, 1971, the end of this investigation, the aftershock rate for M_L larger than 3.0 by that time had dropped to about 1/4 days. Thus this study covers the time period of most of the aftershocks. The question of whether the tectonic activity changes in character after this period even though the aftershock activity is very low is an important subject for future investigation.

The bursts of aftershocks along the west limb during the period between February 21 and April 17 show systematic time-space relationships in themselves. The events within two of the bursts have a systematic sequencing north and south along the west aftershock limb that is not random and must be explained by a causal relationship. Although the relationship may not be as simple as a unidirectional front that triggers events, there is some evidence for a triggering phenomenon that propagates with speeds of 4–15 km/day. These speeds are somewhat high but are comparable to those observed for wave fronts defined by the onset of creep events on the San Andreas fault.

Seismicity in 1961, 1962, and 1969, before the San Fernando series, outlines a linear region extending from Point Dume, near Malibu, in the southwest to Palmdale, on the San Andreas fault, in the northeast. This region exactly coincides with the west aftershock limb and the main shock epicenter. Although the zone is not obviously outlined by mapped geologic structures along its extent, it coincides with some major structural discontinuities such as the fault-controlled west edge of the San Fernando Valley, the sharp north bend of the Santa Susana fault, the down step of the San Fernando fault, and the general trend of left lateral strike slip faulting in the San Gabriel mountains. The history of this zone of weakness is not clear, but it was probably active in the San Gabriel mountain block during Miocene and lower Pliocene, and it is recently active along the western edge of the San Fernando valley. The weakness zone is interpreted as a decoupling boundary between crustal blocks that permits them to deform separately in the prevalent crustal shortening mode of the Transverse ranges region.

REFERENCES

Alewine, R. W., III, and T. H. Jordan, Generalized inversion of earthquake static displacement fields, *Geophys. J. Roy. Astron. Soc.*, in press, 1973.

Allen, C. R., P. St. Amand, C. F. Richter, and J. M. Nordquist, Relationship between seismicity and geologic structure in the southern California region, *Bull. Seismol. Soc. Amer., 55*, 753, 1965.

Allen, C. R., G. R. Engen, T. C. Hanks, J. M. Nordquist, and W. R. Thatcher, Main shock and larger aftershocks of the San Fernando earthquake, February 9 through March 1, 1971, *U.S. Geol. Surv. Prof. Pap. 733*, 17, 1971.

Bailey, T. L., and R. H. Jahns, Geology of the transverse range province, Southern California, Geology of Southern California, *Calif. Div. Mines Geol. Bull., 170*, 83, 1954.

Burford, R. O., R. O. Castle, J. P. Church, W. T. Kinoshita, S. H. Kirby, R. T. Ruthven, and J. C. Savage, Preliminary measurements of tectonic movement, *U.S. Geol. Surv. Prof. Pap. 733*, 80, 1971.

Canitez, N., and M. N. Toksöz, Static and dynamic study of earthquake source mechanism: San Fernando Earthquake, *J. Geophys. Res., 77*, 2583, 1972.

Corbato, C. E., Bouquer gravity anomalies of the San Fernando Valley, California, *Geol. Sci. Publ. 46*, p. 1, Univ. of Calif., Los Angeles, 1963.

Crowell, J. C., Probable large lateral displacement on the San Gabriel fault, southern California, *Amer. Ass. Petrol. Geol. Bull., 36*, 2026, 1952.

Crowell, J. C., Displacement along the San Andreas fault, California, *Geol. Soc. Amer. Spec. Pap. 71*, 61 pp., 1962.

Dillinger, W., and A. F. Espinosa, Preliminary fault-plane solution for the San Fernando earthquake, *U.S. Geol. Surv. Prof. Pap. 733*, 142, 1971.

Division of Geological and Planetary Sciences, California Institute of Technology, Preliminary seismological and geological studies of the San Fernando, California, earthquake of February 9, 1971, *Bull. Seismol. Soc. Amer., 61*, 491, 1971.

Hall, E. A., G. G. Rickels, and W. O. Plant, Oakridge oil field, in *A Guide to the Geology and Oil Fields of the Los Angeles and Ventura Regions*, edited by J. W. Higgins, p. 185, American Association of Petroleum Geologists, Tulsa, Okla., 1958.

Hanks, T. C., A Contribution to the determination and interpretation of seismic source parameters, Ph.D. thesis, 184 pp., Calif. Inst. of Technol., Pasadena, 1972.

Hanks, T. C., T. H. Jordan, and J. B. Minster, Precise locations of aftershocks of the San Fernando earthquake, 2300 (GMT) February 10–1700 February 11, 1971, *U.S. Geol. Surv. Prof. Pap. 733*, 21, 1971.

Healy, J. H., Crustal structure along the coast of California from seismic refraction measurements, *J. Geophys. Res., 68*, 5777, 1963.

Jennings, C. W., and R. G. Strand, Geologic map of California, Los Angeles sheet, Calif. Div. of Mines and Geol., Sacramento, 1969.

Jungels, P., and D. L. Anderson, Strains and tilts associated with the San Fernando earthquake, *U.S. Geol. Surv. Prof. Pap. 733*, 77, 1971.

Jungels, P. H., and G. A. Frazier, Finite element analysis of the residual displacements for an earthquake rupture: Source parameters for the San Fernando earthquake, *J. Geophys. Res., 78*, 5062, 1973.

Kamb, W. B., L. T. Silver, M. J. Abrams, B. A. Carter, T. H. Jordan, and J. B. Minster, Pattern of faulting and nature of fault movement in the San Fernando earthquake, *U.S. Geol. Surv. Prof. Pap. 733*, 41, 1971.

Mellman, G. R., Seismic observations and their tectonic implications for the Pacific-North American plate boundary (abstract), *Geol. Soc. Amer. Abstr. Programs, 4,* 198, 1972.

Oakeshott, G. B., Geology of the Placerita oil field, Los Angeles County, Geology of Southern California, map sheet 31, *Calif. Div. Mines Geol. Bull., 170,* 1954.

Oakeshott, G. B., Geology and mineral deposits of the San Fernando Quadrangle, Los Angeles County, California, *Calif. Div. Mines Geol. Bull., 172,* 147 pp., 1958.

Oliver, H. W., S. L. Robbins, R. B. Grannell, R. W. Alewine, and S. Biehler, Surface and sub-surface movements determined by remeasuring gravity, *Calif. Div. Mines Geol. Bull.,* in press, 1973.

Richter, C. F., Transversely aligned seismicity and concealed structures, *Science, 166,* 173, 1969.

Roth, G. H., and H. H. Sullwold, Jr., Cascade oil field, in *A Guide to the Geology and Oil Fields of the Los Angeles and Ventura Regions,* edited by J. W. Higgins, p. 167, American Association of Petroleum Geologists, Tulsa, Okla., 1958.

Ryall, A., D. B. Slemmons, and L. D. Gedney, Seismicity, tectonism, and surface faulting in the western United States during historic time, *Bull. Seismol. Soc. Amer., 56,* 1105, 1966.

Sanford, A. R., Analytical and experimental study of simple geologic structures, *Geol. Soc. Amer. Bull., 70,* 19, 1959.

U.S. Geological Survey Staff, Surface faulting, *U.S. Geol. Surv. Prof. Pap. 733,* 55, 1971.

Wentworth, C. M., R. F. Yerkes, and C. R. Allen, Geologic setting and activity of faults in the San Fernando area, California, *U.S. Geol. Surv. Prof. Pap. 733,* 6, 1971.

Wesson, R. L., and J. F. Gibbs, Crustal structure in the vicinity of the San Fernando, California earthquake of 9 February, 1971 (abstract), *Eos Trans. AGU, 52,* 804, 1971.

Wesson, R. L., and D. H. Wilson, Faulting in the San Fernando earthquake of February 9, 1971 (abstract), *Eos Trans. AGU, 53,* 449, 1972.

Wesson, R. L., W. H. K. Lee, and J. F. Gibbs, Aftershocks of the earthquake, *U.S. Geol. Surv. Prof. Pap. 733,* 24, 1971.

Whitcomb, J. H., Fault-plane solutions of the February 9, 1971, San Fernando earthquake and some aftershocks, *U.S. Geol. Surv. Prof. Pap. 733,* 30, 1971.